Anthropogenic and climatic contributions to observed carbon system trends in the Northeast Pacific

Ana C. Franco, Debby Ianson, Tetjana Ross, Roberta C. Hamme, Adam H. Monahan, James R. Christian, Marty Davelaar, William K. Johnson, Lisa A. Miller, Marie Robert, and Philippe D. Tortell

2021

Global Biogeochemical Cycles

RESEARCH ARTICLE
10.1029/2020GB006829

Anthropogenic and Climatic Contributions to Observed Carbon System Trends in the Northeast Pacific

Ana C. Franco[1], Debby Ianson[1,2], Tetjana Ross[2], Roberta C. Hamme[3], Adam H. Monahan[3], James R. Christian[2], Marty Davelaar[2], William K. Johnson[2], Lisa A. Miller[2], Marie Robert[2], and Philippe D. Tortell[1,4]

[1]Department of Earth, Ocean and Atmospheric Sciences, University of British Columbia, Vancouver, BC, Canada, [2]Institute of Ocean Sciences, Fisheries and Oceans Canada, Sidney, BC, Canada, [3]School of Earth and Ocean Sciences, University of Victoria, Victoria, BC, Canada, [4]Department of Botany, University of British Columbia, Vancouver, BC, Canada

Key Points:

- Local uptake of anthropogenic CO_2 decreases surface pH in the NE Pacific but the trend appears modulated by recent temporal variability
- Declining ventilation in the NW Pacific appears responsible for 20%–50% of the inorganic carbon increase in NE Pacific intermediate water
- The signature of tidally driven bidecadal oscillations propagates east to Line P producing fluctuations in intermediate water preformed DIC

Supporting Information:

Supporting Information may be found in the online version of this article.

Correspondence to:

A. C. Franco,
afranco@eoas.ubc.ca

Citation:

Franco, A. C., Ianson, D., Ross, T., Hamme, R. C., Monahan, A. H., Christian, J. R., et al. (2021). Anthropogenic and climatic contributions to observed carbon system trends in the northeast Pacific. *Global Biogeochemical Cycles*, *35*, e2020GB006829. https://doi.org/10.1029/2020GB006829

Received 11 SEP 2020
Accepted 10 JUN 2021

Abstract The ocean absorbs anthropogenic carbon, slowing atmospheric CO_2 increase but driving ocean acidification. Long-term changes in the carbon system are typically assessed from single-point time series or from hydrographic sections spaced by decades. Using higher resolution observations (1–3 year^{-1}) from the Line P time series, we investigate processes modulating trends in the carbon system of the northeast subarctic Pacific. Dissolved inorganic carbon (DIC) and apparent oxygen utilization (AOU) from 1990 to 2019 reveal substantial trends over most of the upper water column along the 1,500 km coastal to open ocean transect. At the surface, an increasing trend in salinity-normalized DIC ($sDIC_{33}$) ($+0.5 \pm 0.4$ μmol kg^{-1} yr^{-1}) is associated with a decrease in pH (0.01–0.02 decade^{-1}) and a decrease in aragonite saturation state (0.04–0.08 decade^{-1}). These observed trends are driven by anthropogenic CO_2 uptake, partially offset by trends in surface salinity or temperature. Stratification associated with recent marine heat waves appears to have caused anomalously low surface pCO_2. $sDIC_{33}$ trends of similar magnitude were found below the seasonal thermocline on the 26.7–26.8 isopycnals (150–300 m), which are ventilated in the western Pacific. Roughly, a third (20%–50%) of the subsurface $sDIC_{33}$ trend is driven by increased remineralization, likely caused by long-term decreases in ventilation in the western Pacific. Bidecadal oscillations in the ventilation of the 26.7–26.8 isopycnals arising from the Lunar Nodal Cycle cause oscillations in $sDIC_{33}$ and AOU at the offshore end of our transect. We trace the oscillations to alternating periods of higher anthropogenic carbon uptake or higher carbon remineralization.

Plain Language Summary The ocean takes up anthropogenic carbon and slows the rate at which atmospheric carbon dioxide is increasing. Using 30 years of data from the NE Pacific, we show that the surface ocean is indeed absorbing anthropogenic carbon and undergoing ocean acidification in this region. We find that carbon is also increasing in the subsurface waters. This excess carbon was absorbed in the western Pacific, where dense waters sink from the surface to the subsurface and transport anthropogenic carbon and oxygen eastward. This western Pacific breathing process appears to be weakening in time. If this trend continues, less anthropogenic carbon will be taken up and stored in subsurface waters in the future. Despite this reduction, some carbon will still naturally accumulate as the available oxygen is consumed and natural carbon dioxide is produced. Using data from three decades, we demonstrate the impact of climatic events and natural variability on the carbon system. At the surface, recent marine heat waves have reduced the amount of carbon absorbed by the ocean. In the subsurface waters, we observed that anthropogenic carbon increased in decades with stronger ventilation, while natural carbon generated by respiration of organic matter increased during periods of weaker ventilation.

1. Introduction

The ocean has absorbed a substantial fraction (~30%) of anthropogenic carbon dioxide (CO_2) (Friedlingstein et al., 2019; Sabine et al., 2004), mainly accumulated in regions of deep and intermediate water formation (Gruber et al., 2019; Sabine et al., 2004). Uptake of this additional CO_2 from the atmosphere is the main driver of ocean acidification, a global process in which increasing dissolved inorganic carbon (DIC) concentrations drive decreasing seawater pH and saturation state of calcium carbonate minerals (Ω) (Caldeira

& Wickett, 2003), with varying degrees of impact on the marine environment (Doney et al., 2020; Haigh et al., 2015; Orr et al., 2005; Ross et al., 2020).

Long-term time series (15–30 years) in different ocean regions have documented the direct and indirect impacts of increased atmospheric CO_2 on the carbon system. The surface ocean at most of these sites appears to keep pace with atmospheric CO_2 increases (Bates et al., 2014; Dore et al., 2009). However, concurrent ocean physical and biogeochemical changes have the potential to modulate the overall trends in the seawater partial pressure of CO_2 (pCO_2) and in ocean acidification, as well as the magnitude of CO_2 uptake from the atmosphere (Bates et al., 2014; Dore et al., 2009). For example, analysis of the pCO_2 time series at Station ALOHA, near Hawaii in the subtropical North Pacific, revealed that regional physical variability decreased the strength of the local CO_2 sink over the period 1989–2001 (Dore et al., 2003; C. D. Keeling et al., 2004). Meanwhile, other regions such as the Iceland Sea (Olafsson et al., 2010) or the Munida time series off New Zealand (Currie et al., 2011), have seen a slower increase in surface ocean pCO_2 compared to atmospheric pCO_2 growth (Bates et al., 2014; Currie et al., 2011).

In the North Pacific, increasing surface pCO_2 has mostly followed the atmospheric trend (Takahashi et al., 2006), with regional variations in the strength of the CO_2 sink (Sutton et al., 2017). The northwest Pacific is a significant sink of anthropogenic CO_2 (Sabine et al., 2004; Sutton et al., 2017; Takahashi et al., 2002) driven by the formation and ventilation of intermediate waters, such as the North Pacific Intermediate Water (NPIW) (Talley, 1993). In comparison, CO_2 uptake in the highly stratified northeast Pacific is much weaker and mainly driven by direct ventilation of the shallow upper water column (Sutton et al., 2017; Wong et al., 2010). Below the depth of intermediate waters, some of the oldest waters of the global ocean are found where little anthropogenic carbon has accumulated since the beginning of industrialization (Carter et al., 2019; Clement & Gruber, 2018; Gruber et al., 2019).

An overall decrease in surface salinity (Durack et al., 2012), warming, and increased stratification (Capotondi et al., 2012) may be weakening the shallow overturning circulation of the North Pacific (Ohshima et al., 2014). On top of these long-term changes, natural bidecadal oscillations in the ventilation rate of intermediate water masses have been observed (Ono et al., 2001; Watanabe et al., 2001) and linked to variability in anthropogenic carbon uptake and accumulation in different regions of the North Pacific (Carter et al., 2019; Kouketsu et al., 2013). The anthropogenic signal imprinted in the NPIW is advected into the ocean interior with the potential to rapidly modify the carbon chemistry in distant regions (Resplandy et al., 2013). The significance of these changes has been poorly quantified, particularly in the northeast Pacific.

Here, we aim to quantify long-term changes in the carbon system in the NE Pacific and to disentangle the natural and anthropogenic contributions to such trends. To this end, we make use of 30 years of inorganic carbon measurements from 1990 to 2019 at five time series stations along the Line P longitudinal transect. We first detail our methods, and then present an overview of the vertical and longitudinal distributions of DIC and water masses influencing the transect. We next investigate trends in DIC concentrations and the resulting ocean acidification in surface waters and then along isopycnal surfaces in the subsurface layers. We conclude by examining potential processes linking decadal-scale changes in ocean circulation to decadal variability in the carbon system.

2. Methods

2.1. Line P Observations

Line P is located on the southeastern limb of the Alaskan Gyre, on the northern edge of the California Current (Figure 1a). The transect consists of 26 stations that are usually visited three times per year (typically in February, May/June, and August/September) and extends approximately 1,500 km from the west coast of Canada. The most westerly station (P26; Figure 1a) is also known as Ocean Station P (or Papa, OSP). Here, we analyze trends in DIC and derived parameters (pH, pCO_2, and Ω) obtained at OSP and four other major stations on the transect (P4, P12, P16, and P20; see Figure 1a) from 1990 to 2019 (http://www.waterproperties.ca/linep/).

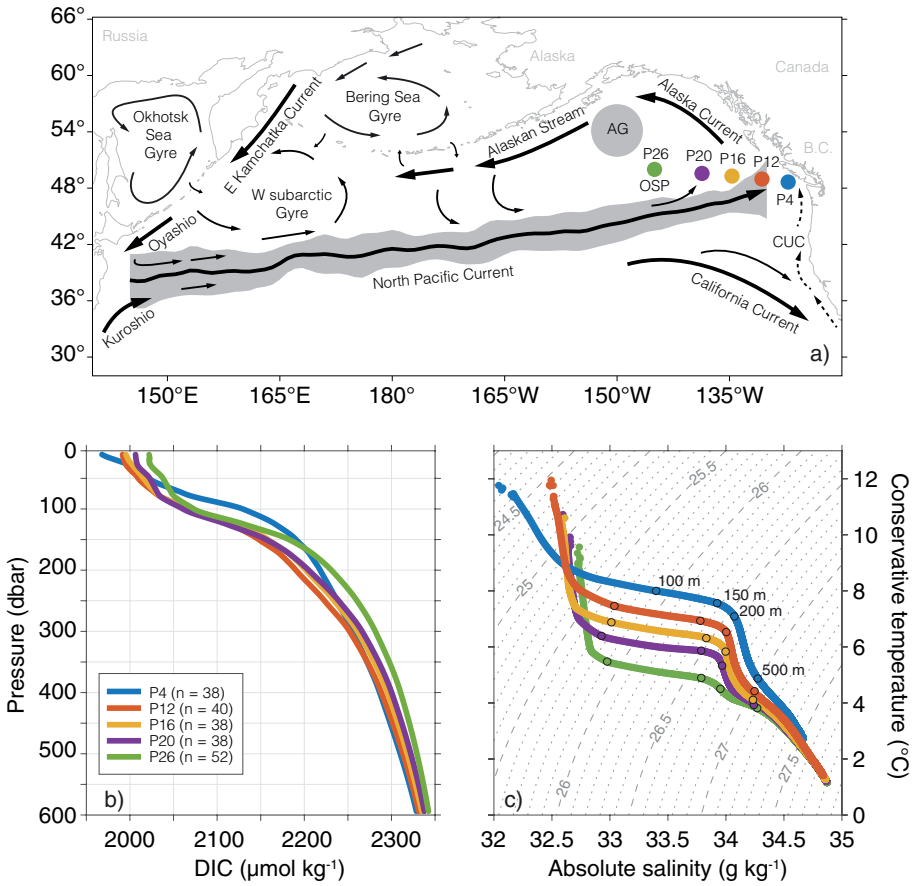

Figure 1. (a) Diagram of the North Pacific Ocean showing the location of the five time series stations along Line P where the inorganic carbon system has been measured routinely. Also shown are the major near-surface currents drawn according to Talley et al. (2011), Thomson (1981), and Whitney et al. (2007). The gray zone around the North Pacific Current (NPC) approximates seasonal and interannual excursions of the core of the NPC, calculated from gridded Argo data (Roemmich & Gilson, 2009) based on a bifurcation streamline analysis similar to Freeland and Cummins (2005). Dashed arrows represent the subsurface flow of the California Undercurrent (CUC) located over a depth range of 150–300 m (Thomson & Krassovski, 2010). (b) Mean vertical profiles of Dissolved Inorganic Carbon (DIC) and (c) mean conservative temperature versus absolute salinity (TEOS-10) diagram averaged for each station, gray lines indicate potential density anomalies (kg m^{-3}). Selected depths are indicated. Colors represent the different stations.

2.1.1. DIC Measurements

DIC samples were collected and analyzed following best practices protocols (Dickson et al., 2007). In short, seawater was collected in standard borosilicate glass bottles, preserved with mercuric chloride ($HgCl_2$), and sealed. DIC was analyzed in the laboratory following the coulometric method (Johnson et al., 1987). We estimated precision based on 141 pairs of duplicate DIC samples collected over the 30-year time series, yielding a pooled standard deviation of ±1.5 μmol kg^{-1}. While DIC has been routinely sampled at Line P since 1986, the use of Certified Reference Materials (CRM) to assess accuracy was not introduced until 1990. Given the sensitivity of the trend calculations to the accuracy of the starting point (Fay & McKinley, 2013), we restrict our analysis to cruises during the period 1990–2019 for which DIC data referenced to the CRM for accuracy are available (Table S1). To remove the effect of long-term salinity changes on the DIC trends, the DIC concentrations were normalized to a constant salinity of 33 ($sDIC_{33}$), approximately the mean salinity in the upper 600 m along the Line P transect.

2.1.2. Oxygen, AOU, and Nutrients

Oxygen concentration in discrete samples was measured at sea by Winkler titration (Carpenter, 1965) with a precision based on replicates (pooled standard deviation) of ±1.4 μmol kg^{-1} (n = 180). From these

measurements, Apparent Oxygen Utilization (AOU) was estimated as the difference between the in situ oxygen concentration and that expected at equilibrium with the atmosphere for the potential temperature and salinity of the water (Garcia & Gordon, 1992, 1993). With few exceptions, dissolved phosphate and silicate were collected concurrently with carbonate system samples. Until February 2010, nutrient analysis was conducted fresh at sea. After 2010, collected samples were returned to the laboratory for analysis. Silicate samples below 400 m were stored at 4 °C in the dark, while the rest of the nutrient samples were stored frozen (Barwell-Clarke & Whitney, 1996). The precision of the dissolved phosphate and silicate data is ±0.03 μmol kg^{-1}(n = 197) and ±1.2 μmol kg^{-1} (n = 210), respectively.

2.2. Data Analysis

We analyzed data from 55 cruises conducted from May 1990 to June 2019 (Table S1). All data are publicly available at the Line P repository (https://www.waterproperties.ca/). Some of these observations were included in the Pacific Ocean Interior Carbon (PACIFICA) data synthesis project (Suzuki et al., 2013), and the associated cruise-specific adjustments were applied (http://pacifica.pices.jp/cgi-bin/PACIFICAadjustment.csv). Each vertical profile was visually inspected, and contrasted with the whole pool of data to detect obvious single-point outliers, which were excluded from the analysis. Following this quality control procedure, more than 200 high-quality DIC profiles were included in the trend analysis, with the number of profiles per time series station ranging from 37 (P20) to 52 (P26). The discrepancies in the number of profiles per station result because some stations were not sampled during a particular cruise. The stations sampled in each cruise are indicated in Table S1. Each profile was then interpolated in depth space to 1 m vertical resolution and in density space to 0.01 kg m^{-3} resolution, using a shape-preserving piecewise cubic interpolation. Density and potential density anomaly (σ_θ) were calculated from CTD-based temperature and salinity profiles with the Thermodynamic Equation of Seawater-2010 (TEOS-10; McDougall & Barker, 2011).

2.2.1. Total Alkalinity Proxy

Over the full 30-year record, the accuracy and precision of the TA observations were variable; thus, we developed an empirical surface TA proxy ($TA_{S,lon}$) by multiple-linear-regression (Wilks, 2011). This proxy depends on practical salinity (S, PSS-78) and longitude (lon, in decimal degrees from −126.5°E to −145.0°E) to capture the increase in salinity normalized TA moving west in the northeast Pacific region (e.g., Fry et al., 2016):

$$TA_{S,lon} = 57.1 * S - 0.537 * lon + 251.53 \quad (1)$$

This relation is valid over the seasonal mixing layer ($S < 33.7$; $n = 98$; $R^2 = 0.93$; standard deviation of the residuals = ±7 μmol kg^{-1}) and was calculated from three recent winter campaigns with robust TA data (2016, 2017, 2019; Figure S1 and Table S2) measured following Dickson et al. (2007). We applied the relationship to all seasons, but we excluded summer data when creating the relationship because coccolithophore blooms, a sink for TA, are common in the Line P region (Lipsen et al., 2007). $TA_{S,lon}$ was calculated only at the surface.

2.2.2. Carbonate System Calculations

The carbonate system was solved at the surface for pH (total scale), pCO_2 and the aragonite saturation state (Ω_a) based on the pair DIC and $TA_{S,lon}$ (for $S < 33.7$), and the corresponding nutrient concentrations, temperature, and salinity using the Matlab version of the CO2SYS program (van Heuven et al., 2011). We used the carbonate dissociation constants of Lueker et al. (2000), the bisulfate ion dissociation constant of Dickson (1990), and the total borate concentration equations of Uppström (1974). Additionally, the routines described in Orr et al. (2018) were used to estimate the combined standard uncertainties in pH (±0.02 pH units), pCO_2 (±17 μatm), and Ω_a (±0.1). Finally, we confirm that our calculated pCO_2 compares well with pCO_2 measured directly in the region (SOCAT database [Bakker et al., 2016]) and shows little or no systematic bias (Figure S2).

2.2.3. Determination of Locally Ventilated Isopycnals

We quantified how often specific isopycnals are locally ventilated (Figure S3) using the latest version of the Roemmich-Gilson Argo Climatology (Roemmich & Gilson, 2009). This product contains monthly

temperature and salinity information binned to a 1 × 1 degree grid. The ventilation timescales were calculated for the boxes closest to the location of the Line P stations by finding the densest surface water observed each winter and generating a probability density function ($n = 17$; years 2004–2020), then fitting a Gaussian distribution to these ventilated densities to estimate the probability of each σ_θ layer returning to the surface within a certain period of time. We consider an isopycnal to be locally ventilated if its ventilation timescale is less than or equal to 10 years. Based on this analysis, we estimate that the isopycnals that outcrop at each Line P station every 10 years are located approximately at the base of the mean winter pycnocline (Figure S4).

2.2.4. Trend Calculations

We calculated the overall trends at the surface (top 10 m) and subsurface on isopycnals present year-round. Surface trends were calculated on time series constructed by averaging together all available discrete samples in the top 10 m for a given station and cruise. At depth, the trends were calculated based on values interpolated onto isopycnal surfaces from discrete sample profiles for each station.

To characterize trends and periodic variability in the time series, a Bayesian Gaussian Process (GP) regression model with constant, linear, and sinusoidal basis functions

$$y(t) = \beta_0 + \beta_1 t + \beta_2 \cos\left(\frac{2\pi t}{T}\right) + \beta_3 \sin\left(\frac{2\pi t}{T}\right) \quad (2)$$

was fit to each time series (Rasmussen & Williams, 2006) using the Matlab function fitrgp. This approach assumes that the model residuals are independent, such that the amplitude parameter of the kernel function was set to be negligible. Non-informative prior distributions were used for the coefficients of the basis functions in order to play a negligible role in the posterior distribution. One of the advantages of the Bayesian GP regression method is that it estimates the full joint posterior probability distributions (assumed to be multivariate Gaussian) of the coefficient set $\{\beta_i\}_{i=1}^{4}$ given an observed time series. The mean and two standard deviation (95% credible interval, [CrI]) of the distribution of the slope parameter β_1 are reported here, representing the overall rate of change in our observations. The CrI in this Bayesian framework is analogous to a frequentist confidence interval and should be interpreted as the 95% probability that the trend lies within the provided range. We considered a trend not to be different from zero when the zero falls within the mean ± 95% CrI range.

Visual inspection of many of the time series show evidence of sinusoidal components, which were characterized well by the GP fit (see Section 4.2.2 and Figure S5). The regression model accounts for known oscillations in the following manner. In Equation 2, T is a constant that stands for the period of the fitted oscillation. At the surface, T was set to a value of 1 year (365.25 days) to account for dominant seasonal variability. Below the locally ventilated isopycnals, T was set to 18.6 years (6,790 days), which corresponds to the period of the Lunar Nodal Cycle (LNC). The signal of the LNC has been detected superimposed on the oxygen and AOU long-term trends in the western and eastern North Pacific (Ono et al., 2001; Sasano et al., 2018; Whitney et al., 2007). If the periodic component is negligible, as occurs for some time series, the value and uncertainty range of the slope are similar to those obtained using only the constant and linear basis functions (first two terms of Equation 2). In those time series where sinusoidal variations are large, not accounting for the periodic component in the regression model results in substantially different estimates of the slope (Table S3).

To test the assumption that the distribution of the residuals is Gaussian (as an a posteriori check of the assumed form of the GP regression model), we used the *p*-value from a Kolmogorov-Smirnov (KS) distribution. By this test, in 98.5% (394 of 400) of the time series analyzed (surface and subsurface), we are not able to reject the assumption (at the 5% significance level) that the distribution of the residuals is Gaussian, supporting the validity of our approach.

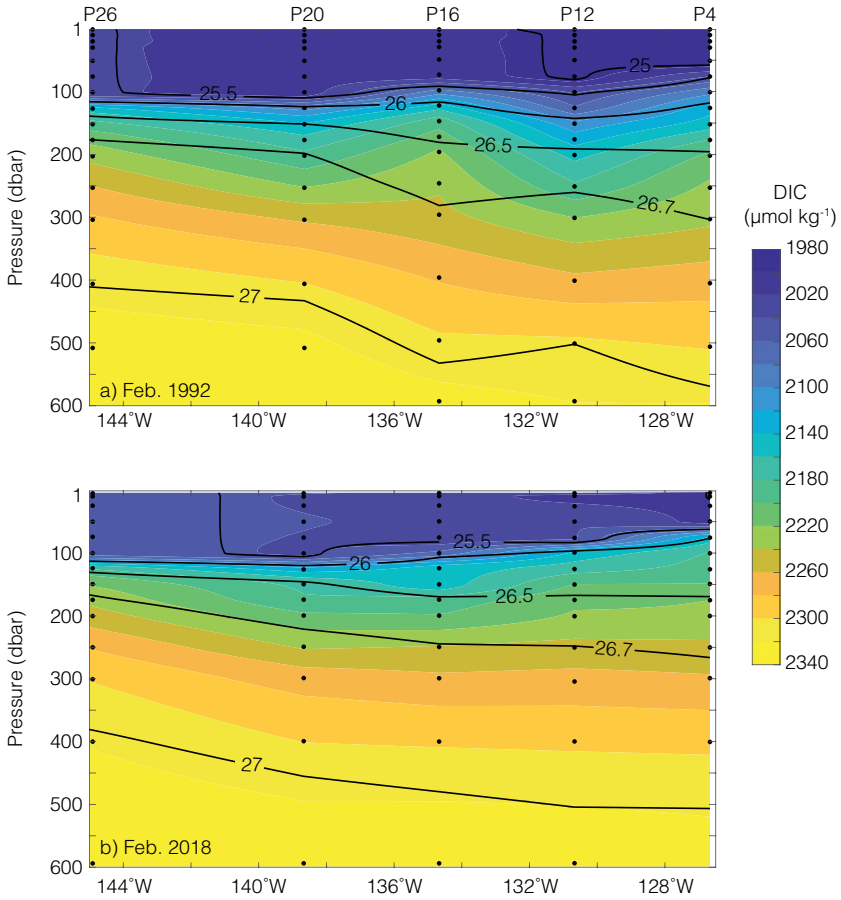

Figure 2. Vertical section of DIC for the winter of (a) 1992 and (b) 2018. Selected σ_θ contours are also shown for comparison. Black dots represent the location of the discrete samples. The station number is indicated on top of panel (a).

3. Hydrography and Inorganic Carbon in the NE Pacific

The confluence of water masses of subarctic and subtropical origin imprints their signal on the biogeochemistry of the Line P region (Thomson & Krassovski, 2010; Whitney et al., 2007). At the surface, mean DIC concentrations are lowest near the coast (<1,970 μmol kg^{-1} at P4), increasing toward the open ocean (Figure 1b). A large fraction of the gradient in DIC is caused by the influence of fresh ($S < 32.5$), low density ($\sigma_\theta < 24.5$ kg m^{-3}) surface waters near the coast (Figure 1c). River input and coastal rainfall sustains this salinity gradient along Line P (Whitney & Freeland, 1999). After accounting for the effect of dilution on DIC by normalizing DIC to a constant salinity ($sDIC_{33}$, $S = 33$), the range in surface concentrations is reduced by more than half (Figure S6a).

DIC increases with potential density and depth, but the vertical DIC and σ_θ gradients in the top 100 m are stronger near the coast than at the more oceanic stations (Figure 2). At the oceanic end of the transect, the mixed layer is deep (approximately 100–120 m in winter [Freeland, 2013]) and decreases toward the coast to a mean winter depth of 75 m (Thomson & Fine, 2003). The potential density anomaly of the water that outcrops in winter also decreases toward the coast, from 25.4 kg m^{-3} at P26 to 24.8 kg m^{-3} at P4, with deeper, denser waters brought to the surface during occasional more severe winters (Figure S3).

Closest to the center of the Alaska Gyre (P26), the influence of colder and fresher subarctic water dominates the characteristics of the water below the seasonal thermocline (Figure 1c). A portion of the subthermocline water in this location can be traced back to the northwest Pacific, where intermediate water is formed and transported eastwards via the North Pacific Current (NPC) (Emerson et al., 2004; Freeland, 2006; Ueno & Yasuda, 2003) (Figure 1a). Toward the coast, mixing with a larger component of warm, high-salinity

Equatorial water transported poleward by the California Undercurrent (CUC), gradually modifies the water properties below the mixed layer (Thomson & Krassovski, 2010). This mixing results in a longitudinal gradient with warmer, saltier water near the coast, and fresher, colder water offshore (Figure 1c).

Near the coast (P4), mean DIC is substantially higher (by approximately 80 μmol kg^{-1}) at 70–150 m depth in comparison with the rest of the stations (Figure 1b). Coastal waters at this depth range have experienced greater amounts of respiration and $CaCO_3$ dissolution (Feely et al., 2016), and the higher DIC is located in a region with lower oxygen concentrations (by about 50 μmol kg^{-1}) and higher nitrate and AOU than the rest of the transect (Figure S6). These signatures have been attributed to a larger influence of the nutrient-rich, low-oxygen waters of the CUC (Thomson & Krassovski, 2010). Additionally, the carbon cycle in the region of P4 is strongly influenced by seasonal summer upwelling and winter downwelling (Ianson et al., 2003).

Over the period from 1990 to 2019, DIC increased with time in both surface and subsurface waters of the subarctic northeast Pacific. To illustrate this change, we contrast winter data (February) of 1992 and 2018 (Figure 2), which are from the first and last cruises in our time series that contain DIC measurements for all five stations. At the surface, DIC is substantially higher in 2018 than in 1992, especially near the coast where salinity and σ_θ have also increased. From the pycnocline to 600 m depth, DIC increased by approximately 10–20 μmol kg^{-1} from 1992 to 2018, causing the DIC isopleths to shoal by approximately 50–100 meters at all stations. This comparison presents an overview of the large changes in DIC occurring in the region, which are consistent with changes observed in other areas of the Pacific basin (Carter et al., 2019; Sabine et al., 2008). However, the two-timeslice comparison between the winter campaigns of 1992 and 2018 provides little information on the temporal dynamics of DIC concentrations, particularly in response to varying circulation at interannual and decadal timescales.

In this paper, we take advantage of the high temporal and spatial resolution of the Line P DIC time series to quantify the contributions of increasing atmospheric pCO_2 and large-scale climatic changes (e.g., changes in salinity [Durack et al., 2012]) in controlling inorganic carbon trends in the NE Pacific. We start our trend analysis at the surface, considering the top 10 m of the water column and continue below the seasonally variable layer, focusing on the top 600 m ($\sigma_\theta < 27.1$ kg m^{-3}), where the largest changes have been observed.

4. Long-Term Trends in the NE Pacific

4.1. Surface Trends in Inorganic Carbon

The surface salinity-normalized DIC concentration ($sDIC_{33}$), measured DIC, and pCO_2 of the NE Pacific increased with time over the period from 1990 to 2019 (Table 1). The $sDIC_{33}$ rate of change was similar at all stations, ranging from 0.5 ± 0.6 μmol kg^{-1} yr^{-1} near the coast (P4), to 0.8 ± 0.4 μmol kg^{-1} yr^{-1} in the middle of the transect (P16). However, trends in salinity cause a longitudinal gradient in the measured (i.e., non salinity-normalized) DIC trend. The rate of DIC increase is highest at P4 (1.2 ± 0.6 μmol kg^{-1}), where salinity is increasing at an overall rate of 0.014 ± 0.010 yr^{-1}, and lowest at P26 (0.3 ± 0.4 μmol kg^{-1} yr^{-1}) in the subarctic gyre (Figure 3), which has become fresher (at a rate of −0.003 ± 0.002 yr^{-1}). This surface freshening has been observed over a longer period of time (since 1956 for P26) (Cummins & Ross, 2020; Freeland, 2013) and is thought to be driven by an intensification of the water cycle as a result of global warming (Durack et al., 2012).

The increase in salinity near the coast (P4, Table 1) could be linked to the influence of large-scale climatic oscillations. Lower upwelling intensity near the mouth of the Juan de Fuca Strait has been correlated with a positive phase of the Pacific Decadal Oscillation (PDO) (Bylhouwer et al., 2013). Upwelling brings water with higher salinity and DIC to the surface (Freeland & Denman, 1982; Ianson et al., 2003). After the first decade of the DIC time series (around year 2000), the PDO transitioned from positive to negative (Trenberth, 2015), potentially driving more intense upwelling and reducing the frequency of low salinity events (which were recorded more frequently over the period from 1960 to approximately 2000; Figure S7). Local observations at six buoys along the shelf confirm trends toward intensification of alongshore wind stress, translating to an increase in both upwelling and downwelling strength (Foreman et al., 2011).

These results highlight the potential impact of large-scale changes in the global water cycle and atmospheric circulation on the carbon system of the upper water column. However, the response of the carbon

Table 1
Observed Trends Per Year and Two Standard Deviation Credible Interval (95% CrI) in Surface Waters

Variable	Station	Trend ± CrI	Std. dev. (*N*)	Eq. trend ± CrI
$sDIC_{33}$ (μmol kg^{-1} yr^{-1})	26	0.5 ± 0.4	20.4 (45)	0.8 ± 0.2
	20	0.5 ± 0.4	22.2 (34)	0.7 ± 0.2
	16	0.8 ± 0.4	25.8 (35)	0.9 ± 0.2
	12	0.6 ± 0.4	20.5 (38)	0.8 ± 0.2
	4	0.5 ± 0.6	30.0 (35)	0.7 ± 0.4
DIC (μmol kg^{-1} yr^{-1})	26	0.3 ± 0.4	25.2 (45)	0.6 ± 0.4
	20	0.5 ± 0.6	25.8 (34)	0.7 ± 0.4
	16	0.5 ± 0.6	30.5 (35)	0.6 ± 0.4
	12	0.5 ± 0.6	26.7 (38)	0.6 ± 0.4
	4	1.2 ± 0.6	41.2 (35)	1.4 ± 0.6
pCO_2 (μatm yr^{-1})	26	1.2 ± 0.8	20.0 (43)	1.87 ± 0.02
	20	1.3 ± 0.6	15.3 (33)	1.89 ± 0.02
	16	1.6 ± 0.8	19.0 (34)	1.86 ± 0.02
	12	1.5 ± 0.6	15.8 (37)	1.92 ± 0.02
	4	1.0 ± 1.4	44.7 (33)	1.86 ± 0.02
pH (yr^{-1})	26	−0.0013 ± 0.0004	0.022 (43)	−0.00197 ± 0.00004
	20	−0.0014 ± 0.0006	0.017 (33)	−0.00191 ± 0.00006
	16	−0.0017 ± 0.0008	0.021 (34)	−0.00197 ± 0.00004
	12	−0.0016 ± 0.0006	0.017 (37)	−0.00199 ± 0.00006
	4	−0.0011 ± 0.0014	0.049 (33)	−0.00181 ± 0.00006
Ω_a (yr^{-1})	26	−0.004 ± 0.002	0.21 (43)	−0.007 ± 0.002
	20	−0.004 ± 0.004	0.23 (33)	−0.006 ± 0.000
	16	−0.008 ± 0.004	0.28 (34)	−0.008 ± 0.002
	12	−0.006 ± 0.004	0.23 (37)	−0.007 ± 0.002
	4	−0.004 ± 0.006	0.29 (33)	−0.007 ± 0.004
Temp. (°C yr^{-1})	26	0.03 ± 0.02	3.22 (48)	
	20	0.03 ± 0.02	3.19 (36)	
	16	0.01 ± 0.02	3.52 (39)	
	12	0.01 ± 0.00	3.52 (42)	
	4	−0.01 ± 0.04	2.68 (39)	
S (PSS-78; yr^{-1})	26	−0.003 ± 0.002	0.119 (49)	
	20	0.0016 ± 0.0006	0.120 (36)	
	16	−0.004 ± 0.004	0.139 (39)	
	12	0.000 ± 0.005	0.205 (42)	
	4	0.014 ± 0.010	0.380 (39)	

Note. Also shown is an estimate of the natural variability, quantified as the standard deviation of all the data points after removing the linear trend with the number of samples used for the calculation (*N*). The last column indicates the expected rate of change assuming equilibrium with atmospheric pCO_2 (obtained from the spatially interpolated product of Landschützer et al., 2020) at observed temperature (Temp), salinity (S), and calculated $TA_{S,Ion}$. The trends were calculated over the period 1990–2019 with two exceptions: P16 (May 1990–March 2018) and P12 (February 1992–June 2019). The trends were calculated accounting for the seasonal cycle.

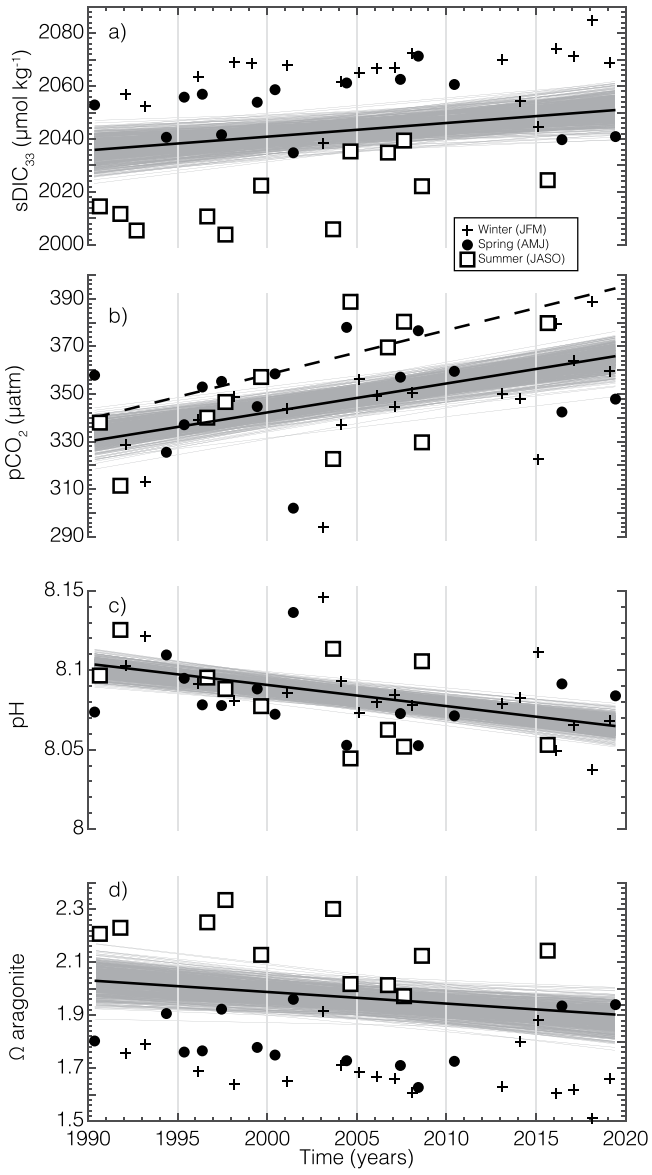

Figure 3. Time series of carbon related parameters averaged over the top 10 m at P26 from 1990 to 2019. (a) Dissolved Inorganic Carbon normalized to a salinity of 33 ($sDIC_{33}$), (b) calculated pCO_2 using measured DIC and $TA_{S,lon}$. The dashed line shows the atmospheric pCO_2 trend at the P26 location derived from Landschützer et al. (2020). (c) In situ pH and (d) saturation state of aragonite. Different markers indicate different seasons. Lines represent trends fitted to all data, accounting for the seasonal cycle. The gray envelopes in the background indicate one standard deviation of the linear trends. Time series of temperature and salinity are shown in Figure S5.

surface trends to climate change is not always straightforward, due to the competing effects of warming, water upwelling from different depths, freshwater fluxes, and the continuous uptake of atmospheric CO_2 superimposed in the DIC and pCO_2 trends. Some of these factors are explored in more detail below.

4.1.1. Local Ventilation and Surface Water CO_2 Uptake

A clear increase in surface water pCO_2 is observed along Line P over the period between 1990 and 2019 (Figures 3 and 4). The pCO_2 trends at all stations are similar, ranging from 1.0 ± 1.4 µatm yr^{-1} at the nearshore end of the transect, to 1.6 ± 0.8 µatm yr^{-1} at the middle station (P16, Table 1). The wide credible interval at P4 is a consequence of the large variability around the trend (Figure 4d and Table 1).

The mean sea surface pCO_2 trends at stations P26 and P20 are notably smaller (although similar within CrI) compared to the pCO_2 trends at transitional stations (P16 and P12). These slower trends (from 1990 to 2019) could be due to the large impact of marine heatwaves that occurred at the end of our time series, in 2013–2016 (Bond et al., 2015) and in 2019 (Amaya et al., 2020). Indeed, when data from spring 2016 and spring 2019 were excluded from the analysis, the mean overall pCO_2 trend of stations P26 and P20 increased to 1.6 ± 0.8 µatm yr^{-1}, which is similar to the rest of the stations and the atmospheric trend.

Our discrete surface ocean pCO_2 was persistently below the atmospheric pCO_2 value at all stations (Figures 3b and 4). Even in winter, when reduced biological production and intensified mixing bring water with high DIC to the surface (Figure 3a), the surface ocean pCO_2 remains below the atmospheric value, in part due to winter cooling (Takahashi et al., 2006). It is also likely that the sampling frequency of our pCO_2 time series does not allow us to capture sporadic supersaturated pCO_2 values that occur in the region (Sutton et al., 2017). Additionally, the marine heatwaves increased stratification (Bond et al., 2015; Whitney, 2015), and likely reduced winter mixing with high DIC subsurface waters, resulting in lower surface pCO_2, particularly in spring 2016 and spring 2019 when some of the largest seasonal anomalies were seen (Figure 3b).

To determine the potential contributions of different factors driving the overall changes in pCO_2 along the transect, we estimate the fraction of the pCO_2 trend given by changes in $sDIC_{33}$, temperature, and freshwater. To this end, we use a first order Taylor expansion (Lovenduski et al., 2007; Sarmiento & Gruber, 2006; Turi et al., 2016) following:

$$\Delta pCO_2 \approx \frac{\partial pCO_2}{\partial DIC}\Delta sDIC_{33} + \frac{\partial pCO_2}{\partial Temp}\Delta Temp + \frac{\partial pCO_2}{\partial fw}\Delta fw \quad (3)$$

where

$$\frac{\partial pCO_2}{\partial fw}\Delta fw = \frac{\partial pCO_2}{\partial S}\Delta S + \frac{\partial pCO_2}{\partial DIC}\Delta DIC_{salt} + \frac{\partial pCO_2}{\partial TA}\Delta TA_{S,lon} \quad (4)$$

The partial derivatives indicate the sensitivity of pCO_2 to each one of the driving components (Table S4). These partial derivative values were calculated by adding and subtracting a small fraction (approximately 1%) of the 30-year mean surface temperature (Temp), Salinity (S), DIC, and alkalinity ($TA_{S,lon}$) and solving the carbonate system for each perturbation and each time series station using the CO2SYS routines (Orr et al., 2018; van Heuven et al., 2011). To estimate the contribution of each parameter, the sensitivities were multiplied by the observed trend in $sDIC_{33}$ and temperature for each station (from Table 1). The freshwater

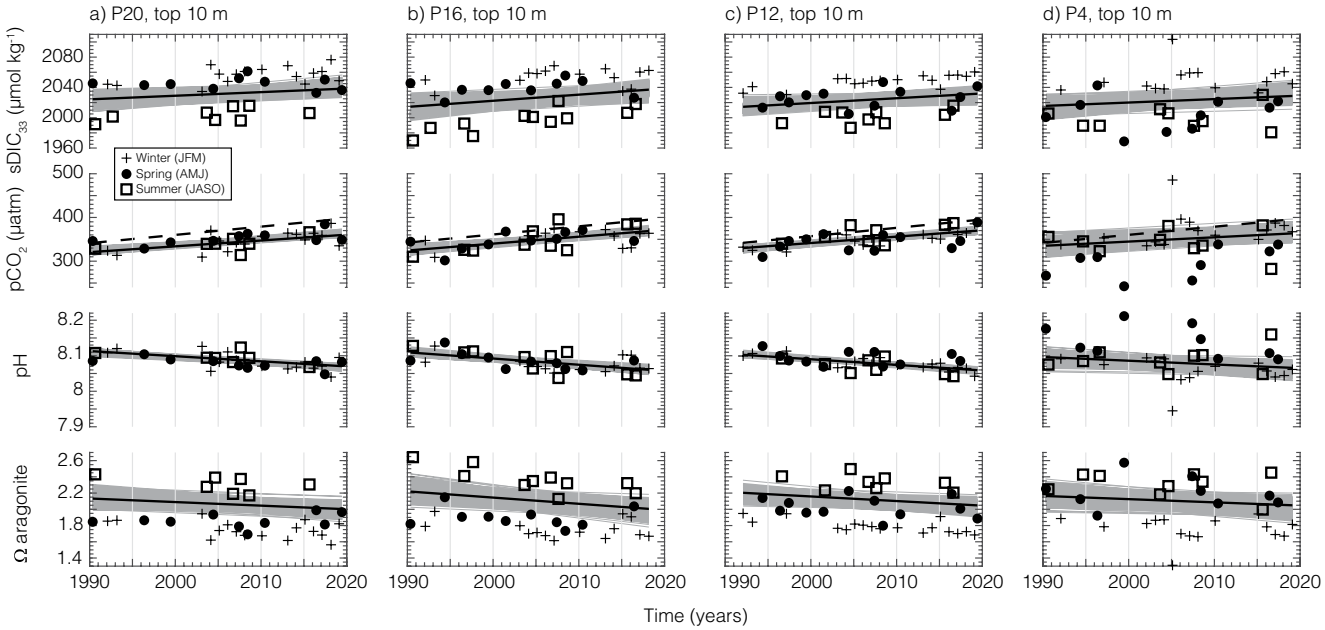

Figure 4. Time series of surface (top 10 m average) $sDIC_{33}$, pCO_2, in situ pH, and Ω_a (rows from top to bottom) at stations (a) P20, (b) P16, (c) P12, and (d) P4. Different markers indicate different seasons. The gray envelopes in the background indicate one standard deviation of the linear trends (solid lines). Also shown is the regional atmospheric pCO_2 trend over the period 1990–2019 (dashed lines), from Landschützer et al. (2020).

(fw) term accounts for the direct effect of changes in salinity on the equilibrium constants, the fraction of changes in DIC driven by changes in freshwater content (represented by ΔDIC_{salt}) and the contribution of the $TA_{S,lon}$ trend. Given that the computed trends in $TA_{S,lon}$ are completely dependent on changes in salinity (see Section 2.2.1), any trend in $TA_{S,lon}$ must be caused by changes in freshwater fluxes.

Results from this analysis show that most of the increase in pCO_2 is driven by increasing $sDIC_{33}$ (Figure 5a). Considering the sensitivity of DIC to changes in ocean pCO_2 (Table S4), we estimate that the main driver of the DIC trends is the continuous uptake of anthropogenic CO_2. In turn, the increase in DIC expected from CO_2 uptake from the atmosphere only is larger (0.9 µmol kg^{-1} yr^{-1}) than the observed $sDIC_{33}$ trends (e.g., 0.5 ± 0.4 µmol kg^{-1} yr^{-1} for P26). This means that other ocean-related processes acting on pCO_2 contribute to a dampening of the observed $sDIC_{33}$ trend.

A substantial warming trend (0.03 ± 0.02 °C yr^{-1}) at the oceanic end of the transect (P26 and P20) enhances the pCO_2 increase with time. On the other hand, our results indicate that the freshwater contribution is negligible despite observed trends in salinity, particularly at opposite ends of the transect (P26 and P4) where the mean salinity trend is larger than the CrI. This occurs mainly because not only the equilibrium constants that govern pCO_2 are not strongly salinity dependent but also the contributions of changing $TA_{S,lon}$ and ΔDIC_{salt} are of similar magnitude but opposite sign.

4.1.2. Implications for Surface Ocean Acidification

The increase in $sDIC_{33}$ and pCO_2 driven by atmospheric CO_2 uptake is accompanied by a corresponding decline in surface pH and Ω_a (Figures 3 and 4). Each of the five time series stations shows decreasing pH trends, which range from −0.0017 ± 0.0008 yr^{-1} at P16 to −0.0011 ± 0.0014 yr^{-1} at P4. However, near the coast the large natural variability is reflected in the largest credible interval, and the trend is not different from zero at the 95% credible interval (Table 1). The total change in pH from 1990 to 2019 amounts to a mean pH decrease of 0.03–0.05 pH units. In absolute terms, the Line P region has moved from an annual mean pH (derived from the fit) of 8.11 in 1990 to a mean pH of 8.06 in 2019.

As with pH and $sDIC_{33}$, the steepest rate of change in Ω_a was calculated at P16 (−0.008 ± 0.004 yr^{-1}), equivalent to a total reduction of 0.2 over the 30 years of observation. In the oceanic region (P26 and P20), not

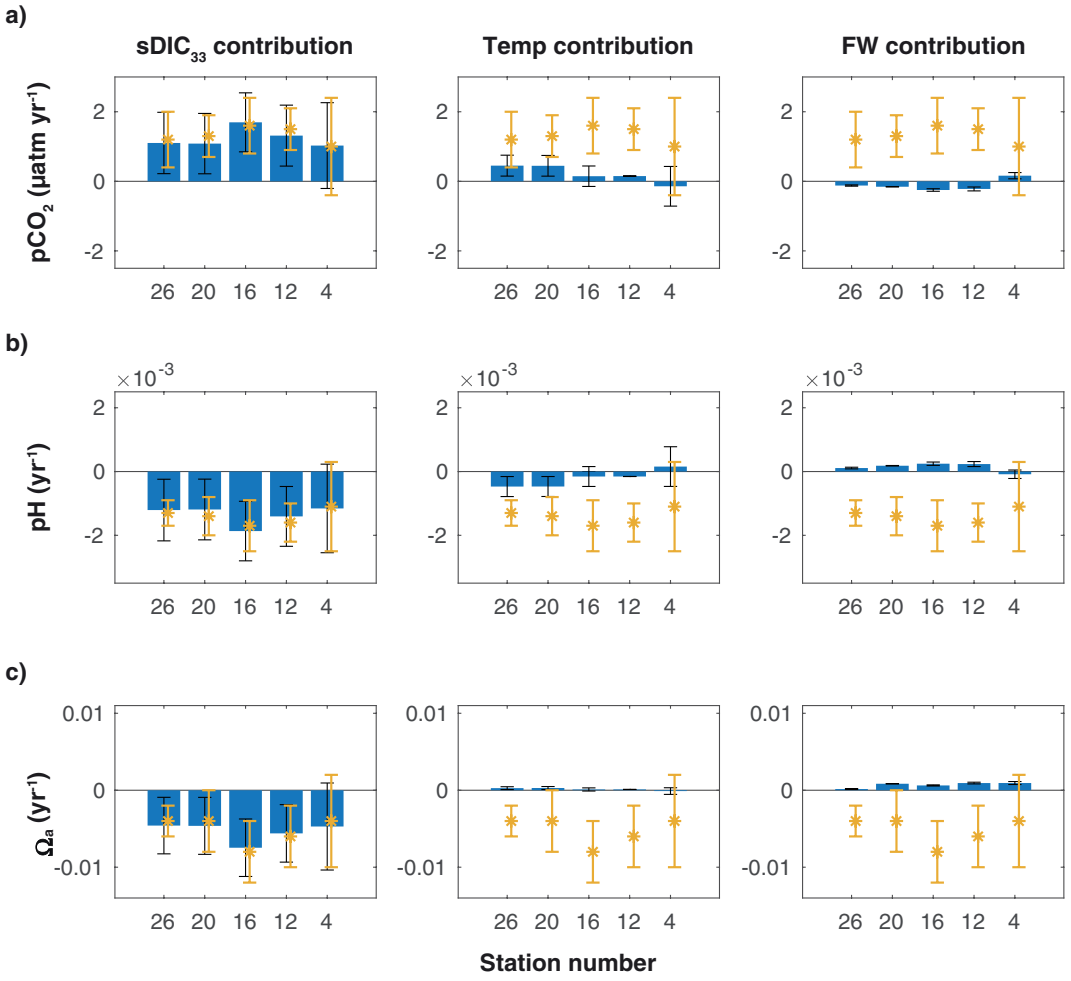

Figure 5. Contribution of surface (top 10 m) changes in $sDIC_{33}$, temperature, and freshwater (FW) to the (a) pCO_2, (b) pH, and (c) Ω_a apparent trends for each station. The total trend and 95% CrI are shown in yellow for each station and are the same as those shown in Table 1.

only the smallest Ω_a trend was found (-0.004 ± 0.004 yr^{-1}) but also the lowest absolute values were recorded, with a mean (derived from the fit) of 1.9 in 2019.

We investigate the impact of the overall trends in $sDIC_{33}$, temperature and salinity on the yearly pH, and Ω_a trends in a similar way as pCO_2 following:

$$\Delta pH \approx \frac{\partial pH}{\partial DIC}\Delta sDIC_{33} + \frac{\partial pH}{\partial Temp}\Delta Temp + \frac{\partial pH}{\partial fw}\Delta fw \tag{5}$$

where

$$\frac{\partial pH}{\partial fw}\Delta fw = \frac{\partial pH}{\partial S}\Delta S + \frac{\partial pH}{\partial DIC}\Delta DIC_{salt} + \frac{\partial pH}{\partial TA}\Delta TA_{S,lon} \tag{6}$$

$$\Delta \Omega_a \approx \frac{\partial \Omega_a}{\partial DIC}\Delta sDIC_{33} + \frac{\partial \Omega_a}{\partial Temp}\Delta Temp + \frac{\partial \Omega_a}{\partial fw}\Delta fw \tag{7}$$

where

$$\frac{\partial \Omega_a}{\partial fw}\Delta fw = \frac{\partial \Omega_a}{\partial S}\Delta S + \frac{\partial \Omega_a}{\partial DIC}\Delta DIC_{salt} + \frac{\partial \Omega_a}{\partial TA}\Delta TA_{S,lon} \tag{8}$$

The largest contribution to the decline in pH and Ω_a is the positive trend of $sDIC_{33}$ (Figures 5b and 5c). At the oceanic stations (P26 to P16), the surface warming trend ($0.03° \pm 0.02°C\ yr^{-1}$) also contributes to the pH decline. While warming causes Ω_a to increase, this trend has a negligible effect on the total change of Ω_a, which, in the open ocean, is entirely driven by changes in $sDIC_{33}$.

Near the coast (P4), changes in $TA_{S,lon}$ largely compensate the changes in DIC driven by changes in freshwater content (encompassed in the freshwater component), while the direct effect of temperature is negligible. Discrepancies between the total trends (Table 1) and the calculated individual contributions (Figures 5b and 5c) are potentially not only due to the linearization of the equation but also the large standard deviations in our estimated trends.

It is unclear how interannual variability (e.g., the PDO), upwelling, or changes in the drivers of the pCO_2 seasonal cycle may affect the apparent CO_2 sink and ocean acidification trends in the NE Pacific. Nonetheless, our results highlight that the spatial variability along Line P can play an important role in setting the absolute trends in the uptake of anthropogenic CO_2 and ocean acidification at each station.

4.2. Drivers of $sDIC_{33}$ Trends in the Water Column

Temporal trends in $sDIC_{33}$ are not confined to the surface. In the water column, positive trends in $sDIC_{33}$ and AOU are found at many densities, with particularly strong trends on the 26.7–26.8 isopycnal layer at most stations (Figure 6). These isopycnals form the core of the North Pacific Intermediate Water (NPIW), which is ventilated in the NW Pacific (Qiu, 1995; Talley, 1991, 1993). The time series at this layer also showed substantial bidecadal variability (Figure 7). This variability is a well known feature of the subpolar North Pacific and has been attributed to the Lunar Nodal Cycle (LNC), with a period of 18.6 years. The LNC has previously been observed in salinity, phosphate, and O_2 in the Oyashio region in the western Pacific (Andreev & Baturina, 2006; Andreev & Kusakabe, 2001; Ono et al., 2001; Osafune & Yasuda, 2006; Sasano et al., 2018) and in the Line P region at P26 (Crawford & Peña, 2016; Emerson et al., 2004; R. F. Keeling et al., 2010; Whitney et al., 2007). We account for the influence of this oscillation on the overall trends by adjusting our harmonic fit equations with a period of 18.6 years (see Section 2.2.4). In the following sections, we first examine the vertical profile of the 30-year $sDIC_{33}$ trends and differences in drivers along the transect. We then discuss decadal variability and its potential influence on the $sDIC_{33}$ trends.

4.2.1. Trends in $sDIC_{33}$, Preformed DIC, and Source Waters

To better understand the processes driving the overall trends in subsurface waters, we make a distinction between the isopycnals that outcrop to the surface at least once every two to 10 years (Figure 6, open markers), and those where ventilation with the atmosphere is restricted to a remote region where the water mass originates (Figure 6, filled markers). The uppermost potential density anomaly shown in Figure 6 was defined as the lightest isopycnal present year round (Figures S3 and S4). Isopycnals that are present only part of the year (i.e., absent in winter) are not shown. Since the depth and potential density anomaly range of the winter pycnocline is variable along the transect, the uppermost σ_θ at each time series is different and ranges from $25.6\sigma_\theta$ at P26 (nearest to the center of the Alaska Gyre) to $25.1\sigma_\theta$ at P4 ($\sim$ 70 km from the coast).

We found a deep maximum in the $sDIC_{33}$ rate of change centered at the 26.7–26.8 isopycnal layer. The magnitude of the $sDIC_{33}$ trend at the 26.7 isopycnal is similar along the transect, ranging from $0.7 \pm 0.4\ \mu mol\ kg^{-1}\ yr^{-1}$ at P4 and P26, to $1.1 \pm 0.6\ \mu mol\ kg^{-1}\ yr^{-1}$ at P16. In this same layer, we detect an apparent increase in AOU at all stations. However, unlike $sDIC_{33}$, there is a longitudinal gradient in the AOU signal. The mean overall AOU trend at the 26.7 isopycnal is weaker at the more oceanic stations P26-P16 ($0.2 \pm 0.4\ \mu mol\ kg^{-1}\ yr^{-1}$) than at the station nearest to the coast, P4 ($0.7 \pm 0.4\ \mu mol\ kg^{-1}\ yr^{-1}$), that has a larger proportion of waters from the eastern tropical North Pacific (Figure 1c).

The 26.7 isopycnal is located at a mean depth of 180 m at the oceanic end of the transect (P26), below the permanent pycnocline. This isopycnal deepens toward the coast, and at P4, it is found at a mean depth of 280 m, on the lower boundary of the California Undercurrent (CUC; Figure 1c; Section 3). A fraction of the water in the $\sigma_\theta = 26.7–26.8$ layer, and extending to the 26.6 isopycnal, has its origin in the North Pacific (Thomson & Krassovski, 2010). Near the Oyashio region, off Japan (Figure 1a), the 26.6 isopycnal outcrops in winter (Mecking et al., 2008; Talley, 1993), where it exchanges gases with the atmosphere. Influenced by

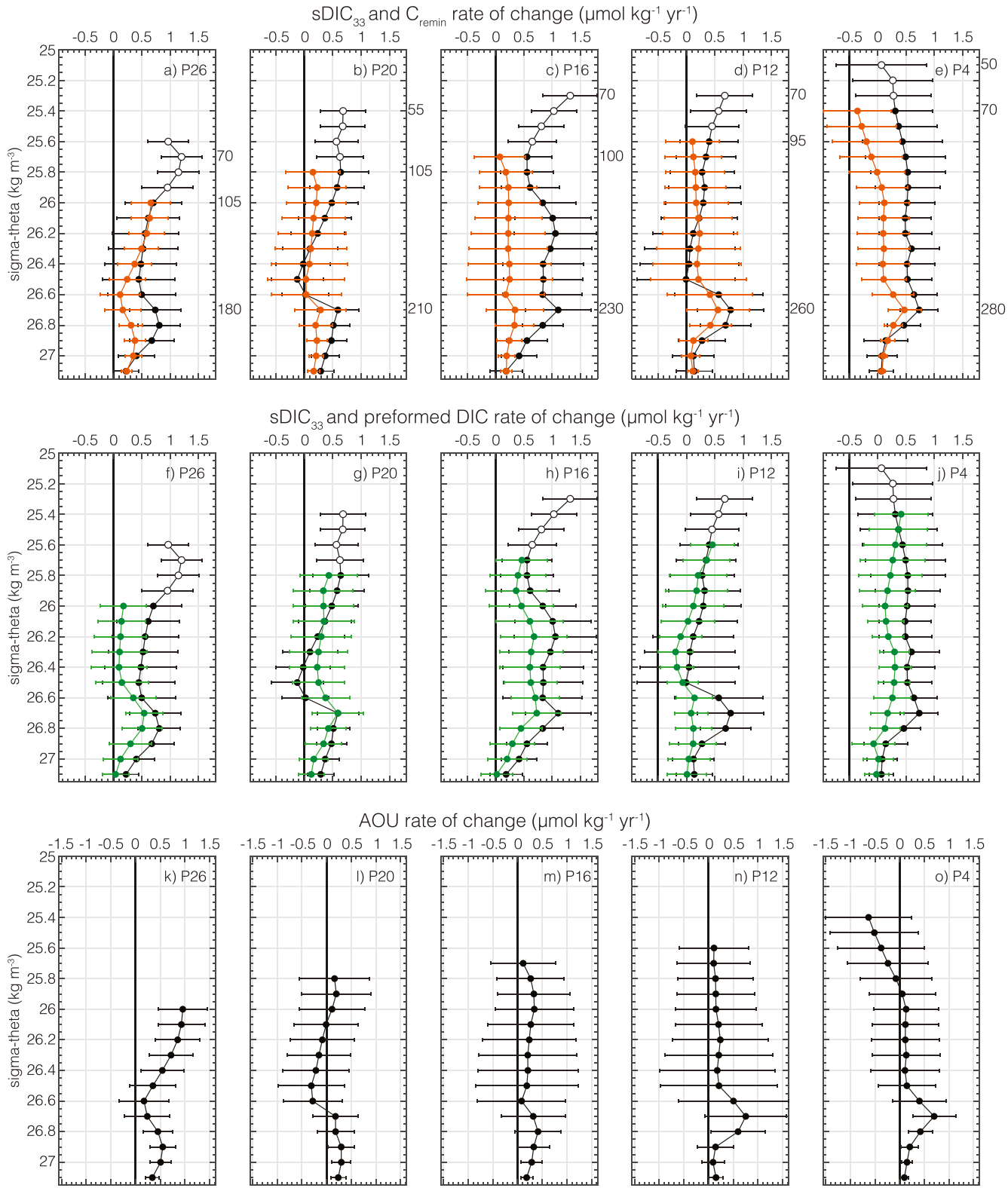

Figure 6. Rate of change in (a–e) $sDIC_{33}$ (black) and C_{remin} (red), (f–j) preformed DIC (green; $sDIC_{pref}$) with $sDIC_{33}$ (black) repeated, and (k–o) AOU (µmol kg^{-1} yr^{-1}), for the period from 1990 to 2019 for each station. Open markers indicate isopycnals that outcrop to the surface at least every 10 years; for C_{remin}, $sDIC_{pref}$, and AOU these isopycnals are not shown. Error bars denote two standard deviations. The mean depth (m) of selected isopycnals is shown on the right axis of the top panel for each station.

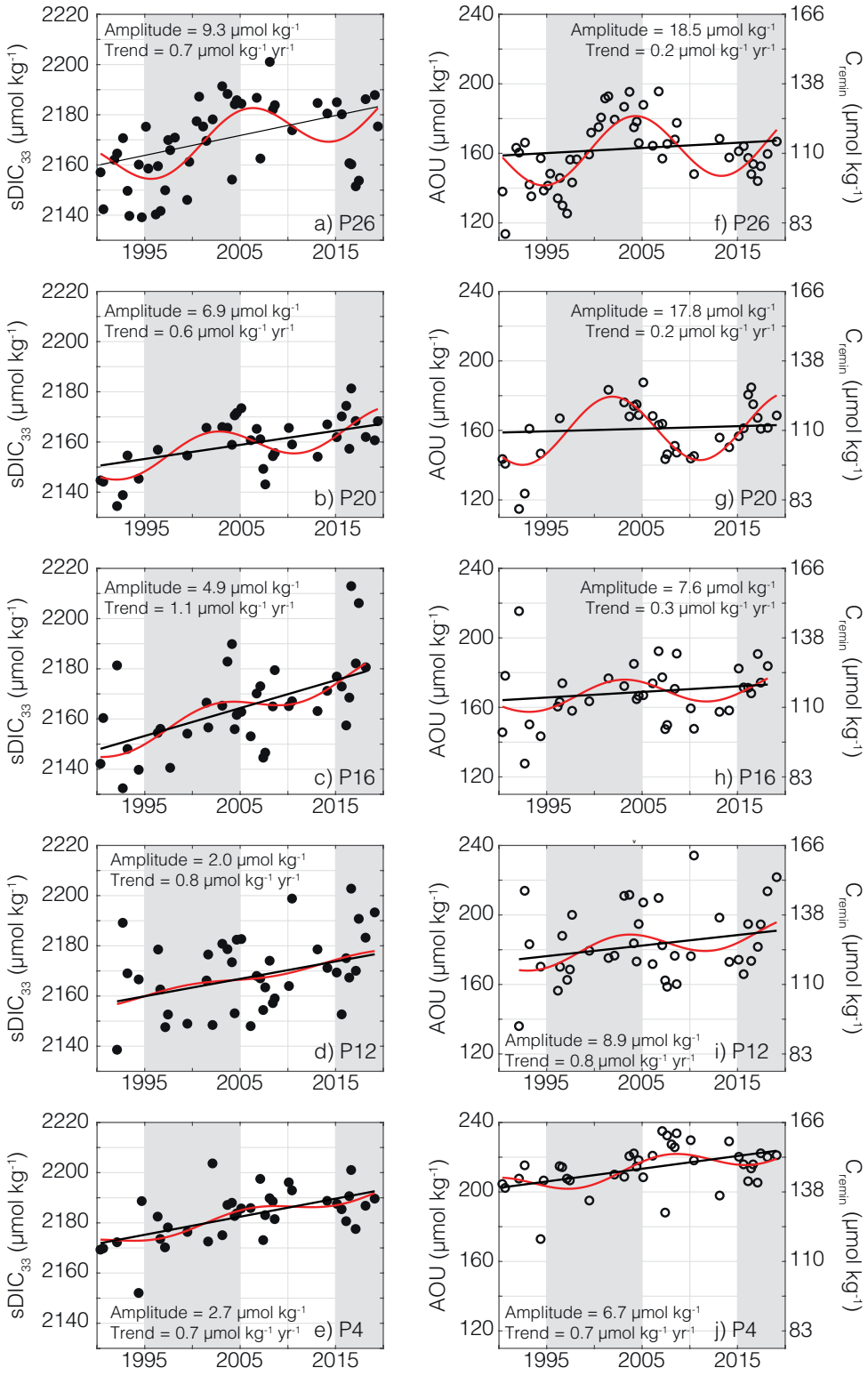

Figure 7. Time series of $sDIC_{33}$ (filled markers), AOU and C_{remin} (open markers) in μmol kg^{-1} interpolated onto the 26.7 kg m^{-3} isopycnal at each station. Black and red lines indicate fitted trends and oscillations, respectively (Equation 2, T = 18.6 years, Section 2.2.4). The value of the $sDIC_{33}$ and AOU trend and amplitude is also shown.

waters from the Sea of Okhotsk, the Kuroshio, and Oyashio currents, this water mass then sinks to intermediate levels where it becomes part of the NPIW. The low salinity, oxygen-rich NPIW moves to the NE Pacific via the North Pacific Current (Figure 1a) and reaches the location of P26 in approximately 7 years (Ueno & Yasuda, 2003; Whitney et al., 2007).

Long-term positive AOU trends of similar magnitude as those reported here (or corresponding negative oxygen trends) have been documented extensively around the 26.7 isopycnal, near the NPIW formation area in the western Pacific (Emerson et al., 2004; Ono et al., 2001; Sasano et al., 2018), at P26 (Cummins & Ross, 2020; Whitney et al., 2007), and along Line P (Crawford & Peña, 2016). This increase in AOU has been attributed to a reduction in ventilation and a weakening in the shallow overturning of the North Pacific (Ono et al., 2001; Sasano et al., 2018). The reduced ventilation is caused by a warming climate, including a rapid decline in sea ice formation in the Sea of Okhotsk (Ohshima et al., 2014). In the NE Pacific, a similar long-term reduction in oxygen concentration was detected in concert with deepening isopycnals below the pycnocline ($\sigma_\theta = 26.6$ to 27.0), suggesting that there is an increased accumulation of these higher AOU waters arriving from the western Pacific (Cummins & Ross, 2020).

Long-term changes in AOU at a specific station may occur because of changes in the age of the water mass (caused by changes in ventilation or circulation speeds) and/or changes in overlying productivity linked to deeper organic matter respiration. Following Ono et al. (2001) and Sasano et al. (2018), we assume that changes in ventilation are the key driver of the AOU trend in our data. The increase in AOU with time is related to a portion of the positive trend in $sDIC_{33}$ by increasing the amount of carbon added to the water mass by remineralization of organic matter (C_{remin}). We estimated the influence of AOU changes on $sDIC_{33}$ as follows:

$$C_{remin} = \gamma_{C:O_2} AOU \tag{9}$$

where $\gamma_{C:O_2}$ is the CO_2 production to O_2 consumption ratio during organic matter remineralization, 117 (±14):170 (±10) (Anderson & Sarmiento, 1994). Assuming the reported uncertainty in the C:O ratio, variations in the C_{remin} trend can amount to approximately 50% the uncertainty of the trends. At the 26.7 isopycnal, the overall increase in C_{remin} varies longitudinally along the transect, and only partially explains the total change in $sDIC_{33}$ (Figures 6a–6e). As with AOU, the C_{remin} trend at the 26.7 isopycnal is weaker in the oceanic section of the transect (e.g., 0.2 ± 0.3 μmol kg^{-1} yr^{-1} at P26) than at the coastal end of the transect (0.5 ± 0.2 μmol kg^{-1} yr^{-1}). In comparison with the total change in $sDIC_{33}$, the C_{remin} trend accounts for approximately 20%–50% of the $sDIC_{33}$ trend for the offshore stations (P26-P16), while it accounts for approximately 70% of the $sDIC_{33}$ trend for the coastal stations. The remaining fraction is consistent with an increasing trend in the concentration of salinity-normalized preformed DIC ($sDIC_{pref}$; Figures 6f–6j) at the region of water mass formation.

We calculated $sDIC_{pref}$, a snapshot of the surface DIC concentration in the formation region, following Murata et al. (2009). First the C_{remin} fraction was subtracted from the concentration of DIC at each available point in time. The resulting difference was then normalized to a constant salinity ($S = 33$) to obtain $sDIC_{pref}$. Once the DIC increase due to remineralization of organic matter (i.e., C_{remin}) is accounted for, any remaining slope in the $sDIC_{pref}$ time series reflects mainly changes in the estimated preformed concentration of $sDIC_{33}$ (when the water was last in contact with the atmosphere), capturing the direct anthropogenic signal of increased atmospheric pCO_2.

At the oceanic end of the transect (P26-P16), a substantial increase in $sDIC_{pref}$ on the 26.7 isopycnal was found (e.g., 0.5 ± 0.4 μmol kg^{-1} yr^{-1} at P26). Despite the suggested long-term decrease in ventilation in the western Pacific (Ohshima et al., 2014), the uptake of anthropogenic CO_2 at the water mass formation region accounts for approximately 70% of the $sDIC_{33}$ increasing trend at P26-P16 in the eastern Pacific (Figures 6f–6h). In absolute terms, $sDIC_{pref}$ has increased by 16 ± 10 μmol kg^{-1} on the 26.7 isopycnal over the period 1990–2019, which is similar to the total $sDIC_{33}$ increase seen at the surface. The direct anthropogenic signal decreases toward the coast (Figures 6i and 6j), where it only accounts for approximately 10%–20% of the total $sDIC_{33}$ trend.

The increase in $sDIC_{pref}$ is roughly consistent with previous estimates of anthropogenic carbon calculated for our study region over different time periods. These previous analyses have used different variations of

Table 2
Trends (μmol kg^{-1} yr^{-1}) in sDIC$_{33}$, sDIC$_{pref}$ and C$_{remin}$ on Selected Isopycnals Over Two 10-Year Periods: 1995–2005 and 2005–2015 for all Stations

Station	Isopycnal	sDIC$_{33}$ ± CrI (1995–2005)	sDIC$_{33}$ ± CrI (2005–2015)	sDIC$_{pref}$ ± CrI (1995–2005)	sDIC$_{pref}$ ± CrI (2005–2015)	AOU ± CrI (1995–2005)	AOU ± CrI (2005–2015)
26	26.7	**3.0 ± 1.6**	0.4 ± 1.7	−0.2 ± 1.3	**2.1 ± 1.0**	**5.4 ± 1.6**	**−1.7 ± 1.8**
	26.8	**3.7 ± 1.3**	0.6 ± 1.6	0.2 ± 1.5	**2.2 ± 1.2**	**5.5 ± 1.0**	**−2.2 ± 1.4**
20	26.7	**1.8 ± 1.0**	0.4 ± 1.2	1.1 ± 1.1	**1.1 ± 1.0**	1.1 ± 1.5	−1.1 ± 1.8
	26.8	**1.9 ± 1.3**	−0.1 ± 0.8	0.2 ± 1.5	**1.2 ± 1.0**	**2.4 ± 1.1**	−2.0 ± 1.2
16	26.7	**2.5 ± 1.9**	1.4 ± 1.4	**2.3 ± 2.0**	**1.6 ± 1.0**	0.9 ± 1.2	−0.4 ± 2.3
	26.8	**2.3 ± 1.9**	0.1 ± 0.7	**2.0 ± 1.8**	1.0 ± 1.0	0.4 ± 1.4	−1.3 ± 1.6
12	26.7	1.9 ± 2.2	0.3 ± 2.0	0.3 ± 1.4	0.9 ± 1.1	**2.9 ± 2.2**	−0.9 ± 3.4
	26.8	**2.3 ± 2.0**	−0.2 ± 1.3	0.6 ± 1.5	0.5 ± 1.2	**2.6 ± 1.7**	−1.1 ± 2.2
4	26.7	1.2 ± 1.3	0.2 ± 1.0	0.8 ± 1.4	0.0 ± 1.0	0.7 ± 1.1	−0.3 ± 2.2
	26.8	**2.0 ± 1.7**	0.1 ± 0.6	**1.7 ± 1.6**	−0.2 ± 0.8	0.2 ± 0.9	0.1 ± 1.1

Note. Also shown is the 95% credible interval of the linear trend. Trends larger than the CrI are indicated in bold.

the Multiple Linear Regression method (Carter et al., 2019; Gruber et al., 2019; Sabine et al., 2008), typically by comparing a minimum of two hydrographic sections separated in time by about a decade. However, our more temporally resolved time series underlying the sDIC$_{33}$ and sDIC$_{pref}$ trends at the 26.7 isopycnal show notable decadal scale variability, particularly at P26 and P20 (Figures 7a and 7b). In the following section, we discuss the role of the LNC signal superimposed on the observed trends at the 26.7–26.8 isopycnal layer.

4.2.2. Remotely Driven Variability in sDIC$_{33}$

At the oceanic stations of Line P, the time series underlying the sDIC$_{33}$ and AOU trends at the 26.7 isopycnal, characteristic of NPIW, are highly correlated (Pearson correlation >0.7) and show bidecadal variability that is tightly linked to the LNC (Figure 7). Similar bidecadal oscillations in O_2 (and AOU) have been recorded in the western North Pacific, and the signal is thought to propagate downstream with the NPC (Crawford & Peña, 2016; Emerson et al., 2004; Mecking et al., 2008; Sasano et al., 2018; Whitney et al., 2007). Thus, it is not surprising that the amplitude of the sDIC$_{33}$ oscillations is maximal at P26 (9.3 μmol kg^{-1}), and decreases gradually toward the coast to P4 (2.7 μmol kg^{-1}) as the influence of water originating in the western Pacific decreases (Figure 7). A similar eastward dampening of decadal oxygen oscillations has been observed (Crawford & Peña, 2016).

To further examine the connectivity between the western and eastern Pacific, we compared the sDIC$_{33}$ time series at P26 at the 26.7 isopycnal with AOU at the same σ_θ obtained from a time series in the Oyashio region in the geographic area defined in Sasano et al. (2018) (Figures S8 and S9). The Oyashio time series leads the P26 time series, and the maximum correlation (Pearson correlation > 0.6) between the P26 sDIC$_{33}$ and Oyashio AOU time series was found when the P26 data were lagged by six years, which approximates the time-scale for water transport from the western to eastern subarctic Pacific (Ueno & Yasuda, 2003; Whitney et al., 2007). This result provides evidence that the DIC concentration in the eastern Pacific can be modified by variations in ventilation in the western Pacific, as previously shown for AOU (Emerson et al., 2004; Mecking et al., 2008). The correlation of AOU in the Oyashio region with sDIC$_{33}$ at our stations decreases considerably with distance from P26 toward the coast (not shown), as the fraction of eastern tropical North Pacific water increases (Figure 1) and coastal processes, like upwelling, influence variability (Section 3).

Over our 30-year time series, a full oscillation cycle was captured in sDIC$_{33}$ and AOU at P26 at the 26.7 isopycnal from 1995 to 2015 (Figures 7a and 7f). During the first decade of the cycle (February 1995–February 2005), sDIC$_{33}$ increased at a rate of 3.0 ± 1.6 μmol kg^{-1} yr^{-1}, while the AOU trend was 5.4 ± 1.6 μmol kg^{-1} yr^{-1} (Table 2). During the following decade (March 2005–August 2015), the AOU trend was negative (−1.7 ± 1.8 μmol kg^{-1} yr^{-1}), while no significant change with time was observed for sDIC$_{33}$ (0.4 ± 1.7 μmol

kg^{-1} yr^{-1}). These oscillations complicate the detection of long-term temporal trends based on end-point comparisons.

The detected bidecadal oscillations have been linked to variability in the ventilation and formation rate of NPIW in the western Pacific. Suggested mechanisms include LNC variations in tidally driven mixing in the Kuril Straits, which affects dense water formation in the Sea of Okhotsk and nearby regions (Ono et al, 2001; Osafune & Yasuda, 2006, 2013). During periods of reduced ventilation, a smaller fraction of recently ventilated water reaches the Oyashio region mixing with a correspondingly larger fraction of re-circulated subtropical water occupying this density layer, thus increasing AOU and $sDIC_{33}$. A substantial portion of the positive trend in $sDIC_{33}$ and AOU during the 1995–2005 period is likely the signal, delayed by 6 years, of weakening tidal mixing. The opposite occurs in 2005–2015 during a period of strengthening mixing, where a progressively larger volume of denser water is ventilated in the Okhotsk Sea.

Periods of reduced NPIW formation have been linked to reductions in uptake of anthropogenic carbon (Watanabe et al., 2001). Indeed, over the 1995–2005 period of reduced ventilation, we estimate a cumulative change in $sDIC_{pref}$ that is smaller than over the following decade when mixing was strengthening (Table 2). From 1995 to 2005, the cumulative (10 years) increase in $sDIC_{33}$ was 30 ± 16 μmol kg^{-1}; however, the majority of this change was driven by a larger amount of C_{remin}. We found a larger contribution of $sDIC_{pref}$ to the $sDIC_{33}$ trend in the following decade (2005–2015) at the stations P26 and P20 (Table 2). Even though $sDIC_{33}$ did not increase during the 2005–2015 period, there was a substantial negative trend in AOU. Periods of time with negative trends in AOU can be related to strengthening ventilation of intermediate waters in the western Pacific (Ueno & Yasuda, 2003; Whitney et al., 2007), which can also lead to increasing uptake of anthropogenic CO_2. The negative AOU trend translates into a reduced contribution of C_{remin} to the total $sDIC_{33}$ change by the end of the period (Figure 7) and a larger accumulation of $sDIC_{pref}$.

5. Summary and Conclusions

Using time series observations of the inorganic carbon system in the northeast Pacific from 1990 to 2019, we have derived new insights into the temporal trends in DIC and ocean acidification in this region. We found that a combination of anthropogenic CO_2 uptake and basin-scale temporal variability influenced the 30-year trends in the carbon cycle over the period from 1990 to 2019.

At the surface, an increasing trend in $sDIC_{33}$ and pCO_2 and a decreasing trend in pH and Ω_a were mostly driven by local uptake of anthropogenic CO_2. At all stations, the sea surface pCO_2 tracked the overall increase in atmospheric pCO_2. However, it is likely that interannual variability (including a series of marine heat waves at the end of the time series) contributed to an apparent recent slow-down in the oceanic pCO_2 growth rate at the oceanic stations P26 and P20. This impact of climate variability on the trends demonstrates the importance of high resolution time series data that can be analyzed for potential bias by specific events.

Below the locally ventilated isopycnals, a substantial positive trend in $sDIC_{33}$ was found and centered around the 26.7 kg m^{-3} isopycnal at all stations (150–300 m). Two processes were found superimposed on the $sDIC_{33}$ trends at the 26.7 kg m^{-3} isopycnal: (a) long-term changes, and (b) tidally driven bidecadal oscillations in its ventilation in the western Pacific. To quantify the contribution of each process to changes in $sDIC_{33}$, we made use of AOU data to examine changes in ventilation and remineralization of organic matter.

The positive 30-year trend found along Line P in AOU on the 26.7–26.8 kg m^{-3} potential density anomaly layer is linked to an overall weakening in the ventilation of NPIW, likely associated with anthropogenic climate warming. Indirectly, these long-term anthropogenic changes in circulation potentially contribute with 20%–50% of the increase in $sDIC_{33}$ at the oceanic end of the transect. Near the coast, there is a smaller fraction of water from the western Pacific and a larger contribution of water from the California Undercurrent, where changes in AOU indicate that increased carbon remineralization contributes approximately 70% of the positive $sDIC_{33}$ long-term trend.

Changes in organic carbon remineralization explain only part of the observed changes in $sDIC_{33}$ below the locally ventilated isopycnals. The remaining long-term increase in $sDIC_{33}$ can be attributed to changes in the preformed concentration of DIC ($sDIC_{pref}$) in the region of water mass origin. In our study region,

intermediate water (150–300 m) is ventilated recently enough to capture the strong upward trend in anthropogenic CO_2. Anthropogenic CO_2 is taken up in the western Pacific and advected to the eastern Pacific via the North Pacific Current. Through this mechanism, increased ventilation decreases AOU and the amount of remineralized DIC, while also potentially capturing a larger amount of anthropogenic carbon and transporting it to the ocean interior. Reduced ventilation has the opposite effect, slowing the uptake of anthropogenic CO_2 while increasing the accumulation of remineralized carbon. The interplay of these two processes was captured in our AOU and DIC time series as a bidecadal oscillation on top of the long-term trend.

On top of the overall trends, bidecadal variations in the ventilation rate of intermediate water masses in the western Pacific generate well-known oscillations in $sDIC_{33}$ and AOU in the eastern Pacific. Over the period 1995–2005, the positive trend in subsurface $sDIC_{33}$ in the NE Pacific was driven by increased remineralization and reduced circulation, potentially caused by sluggish ventilation in the western Pacific, which we detect as a positive trend in AOU in the eastern Pacific. During this decade, we were not able to detect a significant contribution of anthropogenic CO_2 to the long term $sDIC_{33}$ trend. The opposite was true in the following decade. With enhanced ventilation in the region of water mass formation, the uptake of anthropogenic CO_2 increased, but was offset by a decreasing trend in AOU that, in turn, did not generate a significant change in $sDIC_{33}$ over that decade.

Our work serves to illustrate the complex interplay between factors driving carbon system dynamics in the subarctic Pacific and to highlight connections between the western and eastern regions. In the future, with on-going climate change, we expect to see a further reduction in the ventilation of the North Pacific, which can cause a reduced uptake of anthropogenic CO_2 and a larger contribution of DIC from remineralization of organic matter. The results presented here underscore the value of long-term, high quality time series in calculating accurate carbon system trends in the face of large natural oscillations.

Data Availability Statement

The Argo data were collected and made freely available by the International Argo Program and the national programs that contribute to it (http://www.argo.ucsd.edu, http://argo.jcommops.org). All data used in this analysis are publicly available by individual cruise in the Line P repository (https://www.waterproperties.ca/) and as a single synthesis package in the Ocean Carbon Data System (OCADS) with accession number 0234342 (https://www.ncei.noaa.gov/data/oceans/ncei/ocads/metadata/0234342.html).

Acknowledgments
The authors are grateful for the efforts of many individuals who have contributed to the Line P monitoring program, in particular to everyone who has sampled and/or analyzed so many samples over the years, as well as the many crew members of the *CCGS JP Tully*, making these results possible. The pioneering work and foresight of Dr. Chi Shing (C.S.) Wong initiated the collection of inorganic carbon data, and recent funding from Fisheries and Oceans Canada's Aquatic Climate Change Adaptation Service Program has allowed this data collection to continue. The Argo Program is part of the Global Ocean Observing System. Ana C. Franco acknowledges support from the MEOPAR project OxyNet: A network to examine ocean deoxygenation trends and impacts.

References

Amaya, D. J., Miller, A. J., Xie, S.-P., & Kosaka, Y. (2020). Physical drivers of the summer 2019 North Pacific marine heatwave. *Nature Communications*, *11*(1), 1903. https://doi.org/10.1038/s41467-020-15820-w

Anderson, L. A., & Sarmiento, J. L. (1994). Redfield ratios of remineralization determined by nutrient data analysis. *Global Biogeochemical Cycles*, *8*(1), 65–80. https://doi.org/10.1029/93GB03318

Andreev, A. G., & Baturina, V. I. (2006). Impacts of tides and atmospheric forcing variability on dissolved oxygen in the subarctic North Pacific. *Journal of Geophysical Research*, *111*(C7). https://doi.org/10.1029/2005JC003103

Andreev, A. G., & Kusakabe, M. (2001). Interdecadal variability in dissolved oxygen in the intermediate water layer of the Western Subarctic Gyre and Kuril Basin (Okhotsk Sea). *Geophysical Research Letters*, *28*(12), 2453–2456. https://doi.org/10.1029/2000GL012688

Bakker, D. C. E., Pfeil, B., Landa, C. S., Metzl, N., O'Brien, K. M., Olsen, A., et al. (2016). A multi-decade record of high-quality fco_2 data in version 3 of the Surface Ocean CO_2 Atlas (SOCAT). *Earth System Science Data*, *8*(2), 383–413. https://doi.org/10.5194/essd-8-383-2016

Barwell-Clarke, J., & Whitney, F. (1996). Institute of ocean sciences nutrient methods and analysis (Vol. 182). Canadian Technical Report of Hydrography and Ocean Sciences.

Bates, N. R., Astor, Y. M., Church, M. J., Currie, K., Dore, J. E., González-Dávila, M., & Santana-Casiano, J. M. (2014). A time-series view of changing ocean chemistry due to ocean uptake of anthropogenic CO_2 and ocean acidification. *Oceanography*, *27*. https://doi.org/10.5670/oceanog.2014.16

Bond, N. A., Cronin, M. F., Freeland, H., & Mantua, N. (2015). Causes and impacts of the 2014 warm anomaly in the NE Pacific. *Geophysical Research Letters*, *42*(9), 3414–3420. https://doi.org/10.1002/2015gl063306

Bylhouwer, B., Ianson, D., & Kohfeld, K. (2013). Changes in the onset and intensity of wind-driven upwelling and downwelling along the North American Pacific coast. *Journal of Geophysical Research: Oceans*, *118*(5), 2565–2580. https://doi.org/10.1002/jgrc.20194

Caldeira, K., & Wickett, M. E. (2003). Anthropogenic carbon and ocean pH. *Nature*, *425*(6956), 365. https://doi.org/10.1038/425365a

Capotondi, A., Alexander, M. A., Bond, N. A., Curchitser, E. N., & Scott, J. D. (2012). Enhanced upper ocean stratification with climate change in the CMIP3 models. *Journal of Geophysical Research*, *117*, C04031. https://doi.org/10.1029/2011JC007409

Carpenter, J. H. (1965). The Chesapeake Bay Institute technique for the Winkler dissolved oxygen method. *Limnology & Oceanography*, *10*(1), 141–143. https://doi.org/10.4319/lo.1965.10.1.0141

Carter, B. R., Feely, R. A., Wanninkhof, R., Kouketsu, S., Sonnerup, R. E., Pardo, P. C., et al. (2019). Pacific anthropogenic carbon between 1991 and 2017. *Global Biogeochemical Cycles*, *33*(5), 597–617. https://doi.org/10.1029/2018GB006154

Clement, D., & Gruber, N. (2018). The eMLR(C*) method to determine decadal changes in the global ocean storage of anthropogenic CO_2. *Global Biogeochemical Cycles*, *32*(4), 654–679. https://doi.org/10.1002/2017gb005819

Crawford, W. R., & Peña, M. A. (2016). Decadal trends in oxygen concentration in subsurface waters of the Northeast Pacific Ocean. *Atmosphere-Ocean*, *54*(2), 171–192. https://doi.org/10.1080/07055900.2016.1158145

Cummins, P. F., & Ross, T. (2020). Secular trends in water properties at station P in the northeast Pacific: An updated analysis. *Progress in Oceanography*, 102329. https://doi.org/10.1016/j.pocean.2020.102329

Currie, K. I., Reid, M. R., & Hunter, K. A. (2011). Interannual variability of carbon dioxide drawdown by subantarctic surface water near New Zealand. *Biogeochemistry*, *104*(1), 23–34. https://doi.org/10.1007/s10533-009-9355-3

Dickson, A. G. (1990). Thermodynamics of the dissociation of boric acid in synthetic seawater from 273.15 to 318.15 K. Deep Sea Research Part A. *Oceanographic Research Papers*, *37*(5), 755–766. https://doi.org/10.1016/0198-0149(90)90004-F

Dickson, A. G., Sabine, C. L., & Christian, J. R. (2007). Guide to best practices of ocean CO2 measurements (Vol. 3). PICES Special Publication.

Doney, S. C., Busch, D. S., Cooley, S. R., & Kroeker, K. J. (2020). The impacts of ocean acidification on marine ecosystems and reliant human communities. *Annual Review of Environment and Resources*, *45*(1). https://doi.org/10.1146/annurev-environ-012320-083019

Dore, J. E., Lukas, R., Sadler, D. W., Church, M. J., & Karl, D. M. (2009). Physical and biogeochemical modulation of ocean acidification in the central North Pacific. *Proceedings of the National Academy of Sciences*, *106*(30), 12235–12240. https://doi.org/10.1073/pnas.0906044106

Dore, J. E., Lukas, R., Sadler, D. W., & Karl, D. M. (2003). Climate-driven changes to the atmospheric CO_2 sink in the subtropical North Pacific Ocean. *Nature*, *424*(6950), 754–757. https://doi.org/10.1038/nature0188510.1038/nature01885

Durack, P. J., Wijffels, S. E., & Matear, R. J. (2012). Ocean salinities reveal strong global water cycle intensification during 1950 to 2000. *Science*, *336*(6080), 455–458. https://doi.org/10.1126/science.1212222

Emerson, S., Watanabe, Y. W., Ono, T., & Mecking, S. (2004). Temporal trends in apparent oxygen utilization in the upper pycnocline of the North Pacific: 1980-2000. *Journal of Oceanography*, *60*(1), 139–147. https://doi.org/10.1023/B:JOCE.0000038323.62130.a0

Fay, A. R., & McKinley, G. A. (2013). Global trends in surface ocean pCO_2 from in situ data. *Global Biogeochemical Cycles*, *27*(2), 541–557. https://doi.org/10.1002/gbc.20051

Feely, R. A., Alin, S. R., Carter, B., Bednaršek, N., Hales, B., Chan, F., & Juranek, L. (2016). Chemical and biological impacts of ocean acidification along the west coast of North America. Estuarine. *Coastal and Shelf Science*, *183*, 260–270. https://doi.org/10.1016/j.ecss.2016.08.043

Foreman, M. G. G., Pal, B., & Merryfield, W. J. (2011). Trends in upwelling and downwelling winds along the British Columbia shelf. *Journal of Geophysical Research*, *116*(C10). https://doi.org/10.1029/2011JC006995

Freeland, H. J. (2006). What proportion of the North Pacific Current finds its way into the Gulf of Alaska? *Atmosphere-Ocean*, *44*(4), 321–330. https://doi.org/10.3137/ao.44040110.3137/ao.440401

Freeland, H. J. (2013). Evidence of change in the winter mixed layer in the Northeast Pacific Ocean: A problem revisited. *Atmosphere-Ocean*, *51*(1), 126–133. https://doi.org/10.1080/07055900.2012.754330

Freeland, H. J., & Cummins, P. F. (2005). Argo: A new tool for environmental monitoring and assessment of the world's oceans, an example from the N.E. Pacific. *Progress in Oceanography*, *64*(1), 31–44. https://doi.org/10.1016/j.pocean.2004.11.002

Freeland, H. J., & Denman, K. L. (1982). A topographically controlled upwelling center off southern Vancouver Island. *Journal of Marine Research*, *40*, 1069–1093.

Friedlingstein, P., Jones, M. W., O'sullivan, M., Andrew, R. M., Hauck, J., Peters, G. P., et al. (2019). Global carbon budget 2019. *Earth System Science Data*, *11*(4), 1783–1838. https://doi.org/10.5194/essd-11-1783-2019

Fry, C. H., Tyrrell, T., & Achterberg, E. P. (2016). Analysis of longitudinal variations in North Pacific alkalinity to improve predictive algorithms. *Global Biogeochemical Cycles*, *30*(10), 1493–1508. https://doi.org/10.1002/2016GB005398

Garcia, H. E., & Gordon, L. I. (1992). Oxygen solubility in seawater: Better fitting equations. *Limnology and Oceanography*, *37*(6), 1307–1312. https://doi.org/10.4319/lo.1992.37.6.1307

Garcia, H. E., & Gordon, L. I. (1993). Erratum: Oxygen solubility in seawater: Better fitting equations. *Limnology and Oceanography*, *38*(3), 656.

Gruber, N., Clement, D., Carter, B. R., Feely, R. A., van Heuven, S., Hoppema, M., & Wanninkhof, R. (2019). The oceanic sink for anthropogenic CO_2 from 1994 to 2007. *Science*, *363*(6432), 1193–1199. https://doi.org/10.1126/science.aau5153

Haigh, R., Ianson, D., Holt, C. A., Neate, H. E., & Edwards, A. M. (2015). Effects of ocean acidification on temperate coastal marine ecosystems and fisheries in the Northeast Pacific. *PLoS One*, *10*(2), 1–46. https://doi.org/10.1371/journal.pone.011753310.1371/journal.pone.0117533.02

Ianson, D., Allen, S. E., Harris, S. L., Orians, K. J., Varela, D. E., & Wong, C. S. (2003). The inorganic carbon system in the coastal upwelling region west of Vancouver Island, Canada. *Deep Sea Research Part I: Oceanographic Research Papers*, *50*(8), 1023–1042. https://doi.org/10.1016/s0967-0637(03)00114-6

Johnson, K. M., Sieburth, J. M. N., leB Williams, P. J., & Brändström, L. (1987). Coulometric total carbon dioxide analysis for marine studies: Automation and calibration. *Marine Chemistry*, *21*(2), 117–133. https://doi.org/10.1016/0304-4203(87)90033-8

Keeling, C. D., Brix, H., & Gruber, N. (2004). Seasonal and long-term dynamics of the upper ocean carbon cycle at Station ALOHA near Hawaii. *Global Biogeochemical Cycles*, *18*(4). https://doi.org/10.1029/2004gb002227

Keeling, R. F., Körtzinger, A., & Gruber, N. (2010). Ocean deoxygenation in a warming world. *Annual Review of Marine Science*, *2*(1), 199–229. https://doi.org/10.1146/annurev.marine.010908.163855

Kouketsu, S., Murata, A., & Doi, T. (2013). Decadal changes in dissolved inorganic carbon in the Pacific Ocean. *Global Biogeochemical Cycles*, *27*(1), 65–76. https://doi.org/10.1029/2012gb004413

Landschützer, P., Gruber, N., & Bakker, D. C. E. (2020). *An observation-based global monthly gridded sea surface pCO_2 product from 1982 onward and its monthly climatology (NCEI Accession 0160558) (Version 5.5[2020-07-10])*. NOAA National Centers for Environmental Information. Dataset. https://doi.org/10.7289/V5Z899N6

Lipsen, M., Crawford, D., Gower, J., & Harrison, P. (2007). Spatial and temporal variability in coccolithophore abundance and production of PIC and POC in the NE subarctic Pacific during El Niño (1998), La Niña (1999) and 2000. *Progress in Oceanography*, *75*(2), 304–325. https://doi.org/10.1016/j.pocean.2007.08.004

Lovenduski, N. S., Gruber, N., Doney, S. C., & Lima, I. D. (2007). Enhanced CO_2 outgassing in the Southern Ocean from a positive phase of the Southern Annular Mode. *Global Biogeochemical Cycles*, *21*(2). https://doi.org/10.1029/2006GB002900

Lueker, T. J., Dickson, A. G., & Keeling, C. D. (2000). Ocean pCO_2 calculated from dissolved inorganic carbon, alkalinity, and equations for K_1 and K_2: Validation based on laboratory measurements of CO_2 in gas and seawater at equilibrium. *Marine Chemistry*, *70*(1), 105–119. https://doi.org/10.1016/S0304-4203(00)00022-0

McDougall, T., & Barker, P. (2011). Getting started with TEOS-10 and the Gibbs seawater (GSW) Oceanographic Toolbox. *Marine Chemistry*.

Mecking, S., Langdon, C., Feely, R. A., Sabine, C. L., Deutsch, C. A., & Min, D.-H. (2008). Climate variability in the North Pacific thermocline diagnosed from oxygen measurements: An update based on the U.S. CLIVAR/CO2 Repeat Hydrography cruises. *Global Biogeochemical Cycles*, *22*(3). https://doi.org/10.1029/2007gb003101

Murata, A., Kumamoto, Y., Sasaki, K.-I., Watanabe, S., & Fukasawa, M. (2009). Decadal increases of anthropogenic CO_2 along 149°E in the western North Pacific. *Journal of Geophysical Research*, *114*(C4). https://doi.org/10.1029/2008jc004920

Ohshima, K. I., Nakanowatari, T., Riser, S., Volkov, Y., & Wakatsuchi, M. (2014). Freshening and dense shelf water reduction in the Okhotsk Sea linked with sea ice decline. *Progress in Oceanography*, *126*, 71–79. https://doi.org/10.1016/j.pocean.2014.04.020

Olafsson, J., Olafsdottir, S. R., Benoit-Cattin, A., & Takahashi, T. (2010). The Irminger Sea and the Iceland Sea time series measurements of sea water carbon and nutrient chemistry 1983-2008. *Earth System Science Data*, *2*(1), 99–104. https://doi.org/10.5194/essd-2-99-2010

Ono, T., Midorikawa, T., Watanabe, Y. W., Tadokoro, K., & Saino, T. (2001). Temporal increases of phosphate and apparent oxygen utilization in the subsurface waters of western subarctic Pacific from 1968 to 1998. *Geophysical Research Letters*, *28*(17), 3285–3288. https://doi.org/10.1029/2001gl012948

Orr, J. C., Epitalon, J.-M., Dickson, A. G., & Gattuso, J.-P. (2018). Routine uncertainty propagation for the marine carbon dioxide system. *Marine Chemistry*, *207*, 84–107. https://doi.org/10.1016/j.marchem.2018.10.006

Orr, J. C., Fabry, V. J., Aumont, O., Bopp, L., Doney, S. C., Feely, R. A., & Yool, A. (2005). Anthropogenic ocean acidification over the twenty-first century and its impact on calcifying organisms. *Nature*, *437*(7059), 681–686. https://doi.org/10.1038/nature04095

Osafune, S., & Yasuda, I. (2006). Bidecadal variability in the intermediate waters of the northwestern subarctic Pacific and the Okhotsk Sea in relation to 18.6-year period nodal tidal cycle. *Journal of Geophysical Research*, *111*(C5). https://doi.org/10.1029/2005jc003277

Osafune, S., & Yasuda, I. (2013). Remote impacts of the 18.6 year period modulation of localized tidal mixing in the North Pacific. *Journal of Geophysical Research: Oceans*, *118*(6), 3128–3137. https://doi.org/10.1002/jgrc.20230

Qiu, B. (1995). Why is the spreading of the North Pacific intermediate water confined on density surfaces around $\sigma_\theta = 26.8$? *Journal of Physical Oceanography*, *25*(1), 168–80.

Rasmussen, C. E., & Williams, C. K. (2006). *Gaussian processes for machine learning*. MIT Press.

Resplandy, L., Bopp, L., Orr, J. C., & Dunne, J. P. (2013). Role of mode and intermediate waters in future ocean acidification: Analysis of CMIP5 models. *Geophysical Research Letters*, *40*(12), 3091–3095. https://doi.org/10.1002/grl.50414

Roemmich, D., & Gilson, J. (2009). The 2004–2008 mean and annual cycle of temperature, salinity, and steric height in the global ocean from the Argo Program. *Progress in Oceanography*, *82*(2), 81–100. https://doi.org/10.1016/j.pocean.2009.03.004

Ross, T., Du Preez, C., & Ianson, D. (2020). Rapid deep ocean deoxygenation and acidification threaten life on Northeast Pacific seamounts. *Global Change Biology*. https://doi.org/10.1111/gcb.15307

Sabine, C. L., Feely, R. A., Gruber, N., Key, R. M., Lee, K., Bullister, J. L., & Rios, A. F. (2004). The oceanic sink for anthropogenic CO_2. *Science*, *305*(5682), 367–371. https://doi.org/10.1126/science.1097403

Sabine, C. L., Feely, R. A., Millero, F. J., Dickson, A. G., Langdon, C., Mecking, S., & Greeley, D. (2008). Decadal changes in Pacific carbon. *Journal of Geophysical Research*, *113*(C07021). https://doi.org/10.1029/2007jc004577

Sarmiento, J. L., & Gruber, N. (2006). *Ocean biogeochemical dynamics*. Princeton University Press.

Sasano, D., Takatani, Y., Kosugi, N., Nakano, T., Midorikawa, T., & Ishii, M. (2018). Decline and bidecadal oscillations of dissolved oxygen in the Oyashio region and their propagation to the western North Pacific. *Global Biogeochemical Cycles*, *32*(6), 909–931. https://doi.org/10.1029/2017gb005876

Sutton, A. J., Wanninkhof, R., Sabine, C. L., Feely, R. A., Cronin, M. F., & Weller, R. A. (2017). Variability and trends in surface seawater pCO_2 and CO_2 flux in the Pacific Ocean. *Geophysical Research Letters*, *44*(11), 5627–5636. https://doi.org/10.1002/2017gl073814

Suzuki, T., Ishii, M., Aoyama, M., Christian, J. R., Enyo, K., Kawano, T., & Sabine, C. L. (2013). *PACIFICA data synthesis project (ORNL/CDIAC-159, NDP-092)*. Carbon Dioxide Information Analysis Center, Oak Ridge National Laboratory, U.S. Department of Energy. https://doi.org/10.3334/CDIAC/OTG

Takahashi, T., Sutherland, S. C., Feely, R. A., & Wanninkhof, R. (2006). Decadal change of the surface water pCO_2 in the North Pacific: A synthesis of 35 years of observations. *Journal of Geophysical Research*, *111*(C7). https://doi.org/10.1029/2005jc003074

Takahashi, T., Sutherland, S. C., Sweeney, C., Poisson, A., Metzl, N., Tilbrook, B., & Nojiri, Y. (2002). Global sea–air CO_2 flux based on climatological surface ocean pCO_2, and seasonal biological and temperature effects. *Deep Sea Research Part II: Topical Studies in Oceanography*, *49*(9), 1601–1622. https://doi.org/10.1016/s0967-0645(02)00003-6

Talley, L. D. (1991). An Okhotsk Sea water anomaly: Implications for ventilation in the North Pacific. *Deep Sea Research Part A: Oceanographic Research Papers*, *38*, S171–S190. https://doi.org/10.1016/S0198-0149(12)80009-4

Talley, L. D. (1993). Distribution and formation of North Pacific intermediate water. *Journal of Physical Oceanography*, *23*(3), 517–537. https://doi.org/10.1175/1520-0485(1993)0230517:DAFONP2.0.CO;2

Talley, L. D., Pickard, G. L., Emery, W. J., & Swift, J. H. (2011). *Descriptive physical oceanography: An introduction*. Academic Press.

Thomson, R. E. (1981). Oceanography of the British Columbia coast. *Canadian Special Publication of Fisheries and Aquatic Sciences*, *56*, 291.

Thomson, R. E., & Fine, I. V. (2003). Estimating mixed-layer depth from oceanic profile data. *Journal of Atmospheric and Oceanic Technology*, *20*, 319–329. https://doi.org/10.1175/1520-0426(2003)020<0319:emldfo>2.0.co;2

Thomson, R. E., & Krassovski, M. V. (2010). Poleward reach of the California Undercurrent extension. *Journal of Geophysical Research*, *115*(C9). https://doi.org/10.1029/2010JC006280

Trenberth, K. E. (2015). Has there been a hiatus? *Science*, *349*(6249), 691–692. https://doi.org/10.1126/science.aac9225

Turi, G., Lachkar, Z., Gruber, N., & Münnich, M. (2016). Climatic modulation of recent trends in ocean acidification in the California Current System. *Environmental Research Letters*, *11*(1), 014007. https://doi.org/10.1088/1748-9326/11/1/014007

Ueno, H., & Yasuda, I. (2003). Intermediate water circulation in the North Pacific subarctic and northern subtropical regions. *Journal of Geophysical Research*, *108*(C11). https://doi.org/10.1029/2002jc001372

Uppström, L. R. (1974). The boron/chlorinity ratio of deep-sea water from the Pacific Ocean. *Deep Sea Research and Oceanographic Abstracts*, *21*(2), 161–162. https://doi.org/10.1016/0011-7471(74)90074-6

van Heuven, S., Pierrot, D., Rae, J. W. B., Lewis, E., & Wallace, D. W. R. (2011). *MATLAB program developed for CO2 system calculations (Technical Report ORNL/CDIAC-105b)*. Carbon Dioxide Information Analysis Center, Oak Ridge National Laboratory, U.S. Department of Energy. https://doi.org/10.3334/CDIAC/otg

Watanabe, Y. W., Ono, T., Shimamoto, A., Sugimoto, T., Wakita, M., & Watanabe, S. (2001). Probability of a reduction in the formation rate of the subsurface water in the North Pacific during the 1980s and 1990s. *Geophysical Research Letters*, *28*(17), 3289–3292. https://doi.org/10.1029/2001gl013212

Whitney, F. A. (2015). Anomalous winter winds decrease 2014 transition zone productivity in the NE Pacific. *Geophysical Research Letters*, *42*(2), 428–431. https://doi.org/10.1002/2014GL062634

Whitney, F. A., & Freeland, H. J. (1999). Variability in upper-ocean water properties in the NE Pacific Ocean. *Deep-Sea Research Part II: Topical Studies in Oceanography*, *46*, 2351–2370. https://doi.org/10.1016/s0967-0645(99)00067-3

Whitney, F. A., Freeland, H. J., & Robert, M. (2007). Persistently declining oxygen levels in the interior waters of the eastern subarctic Pacific. *Progress in Oceanography*, *75*(2), 179–199. https://doi.org/10.1016/j.pocean.2007.08.007

Wilks, D. S. (2011). *Statistical methods in the atmospheric sciences* (3rd ed.). Academic Press.

Wong, C. S., Christian, J. R., Emmy Wong, S.-K., Page, J., Xie, L., & Johannessen, S. (2010). Carbon dioxide in surface seawater of the eastern North Pacific Ocean (Line P), 1973–2005. *Deep Sea Research Part I: Oceanographic Research Papers*, *57*(5), 687–695. https://doi.org/10.1016/j.dsr.2010.02.003